Cell-cell communication controls the timing of gastruloid symmetry-breaking

David Oriola[1,2,*], Gabriel Torregrosa-Cortés[3,*], Krisztina Arató[1], David Fernández-Munuera[1], Elisa Maria Hahn[1], Kerim Anlaş[1], Jordi Garcia-Ojalvo[2,3] & Vikas Trivedi[1,2,4]

[1]EMBL Barcelona, Barcelona Biomedical Research Park, 08003, Barcelona, Spain
[2]Barcelona Collaboratorium for Modelling and Predictive Biology, 08005 Barcelona, Spain
[3]Department of Medicine and Life Sciences, Universitat Pompeu Fabra, Barcelona Biomedical Research Park, 08003 Barcelona, Spain
[4]EMBL Heidelberg, Developmental Biology Unit, 69117 Heidelberg, Germany
[*]These authors contributed equally to this work

In the embryo, morphogenetic signals instruct regional patterning thereby defining the body axes of the future animal. Remarkably, in the absence of such signals, collections of pluripotent stem cells can still self-organise and break symmetry *in vitro*. One such example is gastruloids, three-dimensional stem cell aggregates that form an anterior-posterior axis through the polarised expression of the gene Brachyury/T. How robust and reproducible cell proportions are achieved in these self-organised embryo-like structures is not understood. Here, through quantitative experiments and theoretical modelling, we dissect tissue rheology and cellular feedback in gastruloids. We show that the initial population of Brachyury-expressing cells critically influences the timing of symmetry-breaking. We propose a cell differentiation model, whereby pluripotent cells inhibit mesoderm differentiation, accounting for the observed cell fate dynamics. Our findings suggest that cell-cell communication dictates temporal cell proportions, while differential tissue mechanics governs spatial pole formation. Our work highlights the importance of initial cell heterogeneity in gastruloid development and offers a framework to identify feedback mechanisms in multicellular systems, advancing our understanding of how embryo-like structures self-organise.

Introduction

How animals establish the body plan is a fundamental problem in biology (*1,2*). Molecular cues, such as those coming from extra-embryonic tissues, polarise the early embryo thereby breaking symmetries and generating a coordinate system for subsequent regional patterning (*3–7*). In the last decade, several studies have demonstrated that collections of stem cells can break symmetry *in vitro* even in the absence of instructive signals (*8*). Such examples are found in rostral-caudal (*9*), anterior-posterior (*10, 11*), and dorsal-ventral (*12*) patterning. In particular, 3D gastruloids (*11, 13–15*) have emerged as a robust model system to study the spontaneous formation of the primary body axis *in vitro*. While several candidate mechanisms such as reaction-diffusion (*8, 16*), tissue flows (*17*) or cell sorting (*18–20*) have been proposed to explain symmetry breaking, a major challenge is to understand how robust cell proportions are controlled in the system (*21–24*). In particular, it is still unknown how cells coordinate their biochemical and mechanical activities during symmetry breaking to achieve the right cell proportions in space and time.

Here we use cell proportion experiments in combination with single-cell RNA sequencing analysis, biophysical measurements and mathematical modelling to understand cell fate dynamics during gastruloid symmetry breaking. By studying aggregates composed of different initial amounts of cells expressing Brachyury/T (T+ cells), we show that the timing of symmetry breaking and subsequent gastruloid elongation is highly dependent on the initial T+ cell population. Prior to polarisation, we find that T- cells are enriched in the periphery of the aggregates while T+ cells are found in the core. Spatial differences in the localisation of the tissues correlate with differences in surface tension between the T+ and T- cell aggregates, suggesting a cell sorting mechanism involved in symmetry-breaking. Finally, we show that a cell differ-

entiation model whereby the pluripotent cell population inhibits the differentiation of the T+ cells accounts for the observed cell fate dynamics. Overall, our work sheds light into the self-organisation of 3D embryo-like structures and provides a systematic method to dissect cellular feedbacks *in vitro*.

Results

T population dynamics is dependent on the initial fraction of T+ cells in gastruloids

The canonical gastruloid protocol consists on the aggregation of ~ 300 mouse embryonic stem cells (mESC) followed by a 24h CHIR-99021 (CHIR) pulse at 48 hours post aggregation (hpa) (*11, 13, 25*). Gastruloids polarise around 72 hpa and rapidly elongate at 96 hpa. Heterogeneity on the levels of T or Wnt signalling at 24 hpa are known to increase the variability in gastruloid formation (*11, 20, 26–28*). However, the underlying reasons for these differences remain unknown. In order to understand the robustness of the symmetry breaking process, we varied the initial amount of T+ cells in a controlled manner while seeding cells for gastruloid formation. Unlike the canonical gastruloid protocol, we decided to grow gastruloids in the absence of a CHIR pulse (*29, 30*) to study the inherent signalling dynamics of cells. We used an E14 Bra/T::GFP cell line to visualise T expression and cells were maintained in ES-Lif (ESLIF) medium. In these conditions, typically $\lesssim 5\%$ of cells differentiate to become T+ (see Methods). We took advantage of this fact to sort T+ and T- cells from culture via fluorescence-activated cell sorting (FACS) and generate 3D aggregates with controlled T+ fractions. T+ and T- cells were mixed in different proportions to form 3D cell aggregates in ultra-low adherence multiwell plates (Fig. 1A). By using the GFP signal as a proxy for the T+ cell population, we estimated the fraction of T+ cells over time, $\phi(t)$ (Fig. 1B,C,D, Fig. S1A and Methods). While tissue polarisation was observed in all cases, the time of polarisation varied depending on the initial

T+ fraction (Fig. 1C and Fig. S1C). The change in T dynamics depending on the inital T+ fraction became more evident when the average fraction of T+ cells (ϕ) was plotted as a function of the initial T+ fraction ($\phi(0)$) at 24, 48 and 72 hpa (Fig. 1D). Cell aggregates that were initially formed with a large amount of T+ cells ($\phi \gtrsim 0.5$) polarised and elongated at 48 hpa instead of at 72 hpa (Fig. 1B,C and Fig. S1B,C). The fact that a high T+ population favors rapid polarisation is analogous to the high expression of T+ cells following the addition of CHIR in the canonical protocol, which leads to fast polarisation and elongation (*11, 13*). Notably, the timing and degree of elongation were also affected depending on the initial T+ fraction (Fig. 1E and Fig. S1B). We thus conclude that the initial fraction of T+ cells at the time of seeding crucially determines the timing of gastruloid polarisation and elongation.

Single-cell RNA-seq allows the identification of the major cellular states during early gastruloid differentiation

The cellular identity of T- (GFP-) cells in our experiments is compatible with both a pluripotent state as well as with a differentiated mesoderm state in which T expression was lost. In order to discern between these two cases and to allow for the identification of the major cellular states, we made use of our previously published single-cell RNA sequencing dataset (*29*). We focused on the cell fate dynamics from 24-48 hpa by integrating both time points (Fig. 2A, gray data points in the background). Given the challenges of classical clustering and annotation approaches to split states with subtle gene modifications, we decided to use a custom annotation approach (see Material and Methods) using cell fate markers known in the literature. Using this method, we annotated the major cellular fates and their proportions, as well as their time evolution trajectories (Fig. 2A,B, Figs. S2, S3 and Table S1). Compared to other methods which require many annotation markers (*31*), our simple method provides a robust approach more suitable for the annotation of continuous processes with small transcriptomic differences. We

further validated the consistency of our annotation approach with traditional clustering methods, showing good agreement between communities discovered and annotation (see Fig. S2B, C, E). At 24 hpa, approximately one-third of the cells were found in an epiblast/pluripotent state (Nanog+, Sox2+) while the remaining two-thirds started transitioning to primitive streak-like states (see Fig. 2A and Fig. S2D). A large population of those differentiated cells ($\simeq 63\%$) were Nanog+, T+, which we may refer to as posterior epiblast-like. The remaining fraction of differentiated cells consisted mainly on a Nanog-, T+ population ($\simeq 31\%$) referred to as a posterior primitive-streak-like state and only a minority of cells ($\simeq 6\%$) were found in anterior mesoderm-like (Eomes+, Gata6+, Mesp1+) or endoderm-like (Eomes+, Gata6+, Sox17+) states (see Fig. 2A). The scenario at 48 hpa showed an increase of the posterior primitive streak-like population (Nanog-, T+) coming from cells differentiating from the posterior epiblast-like state. Finally, the differentiation of Nanog-, T+ cells contributed to the emergence of a posterior mesoderm-like state (Aldh1a2+, Tbx6+) (see Fig. 2A, C, S2). Overall, the previous results recapitulate an analogous progression of the bifurcation tree observed in the mouse embryo (*32*). A similar analysis on a second replicate experiment resulted in the same conclusions stated above (see Fig. S3).

To verify the progression and the spatial patterning of the previously identified cellular states, we performed RNA hybridization chain reaction (HCR) stainings. Given that experimentally we have access to the dynamics of the T+ state, we broadly classify all cell types into 3 states: Nanog+ pluripotent state (state A, cluster 1), T+ primitive streak-like state (state B, clusters 2 and 3) and further differentiated states Aldh1a2+ and Gata6+ (state C, clusters 4,5 and 6). We stained for markers of these states at 24, 48 and 72 hpa in gastruloids (Fig. 2D,E and Fig. S4) and on purely T- ($\phi = 0$) and T+ ($\phi = 1$) FACS sorted aggregates (Fig. S5). Nanog was homogeneously distributed at 24 hpa for both control gastruloids and T- sorted aggregates

and was found in small clusters in the anterior region at 72 hpa (see Figs. 2D,S4 and S5). Conversely, T+ sorted aggregates showed low Nanog expression at 24 hpa and no expression at 48 hpa, with structures resembling small 72 hpa gastruloids (Fig. S5). We thus conclude that T+ cells (state B) cannot differentiate back to the pluripotent state (Nanog+, state A). Interestingly, we observed that the cells in state C (expressing Aldh1a2 and/or Gata6) were restricted to the periphery in both gastruloids (Fig. 2D) and T- sorted aggregates at 48 hpa (Fig. S4, S5). Similarly, Aldh1a2 and Gata6 were preferentially found on the periphery of the 24 hpa T+ sorted aggregates (see Fig. S5). At 72 hpa, Aldh1a2 and Gata6 were found in the anterior region of T- sorted aggregates and gastruloids, consistent with previous work (*13, 29*). Overall, our results show that early signs of radial symmetry breaking on T expression are already present at 48 hpa, prior to proper gastruloid polarisation at 72 hpa.

T- cells are enriched on the periphery of the 3D aggregates in cell proportion experiments

The previous HCR stainings show that state C (T-) cells form clusters on the periphery of 48 hpa gastruloids while state B (T+) cells are found on the core (Fig. 2D). Given recent evidences of cell sorting in gastruloids depending on Wnt (an upstream T regulator) activity (*20*), we decided to explore if state A cells (T-) would also be restricted to the periphery of the aggregates in our cell proportion experiments. Given that our cell line had a single cell reporter (Bra::GFP), it was not a priori possible to distinguish A-B from B-C transitions. In order to circumvent this problem, we made use of exogenous labelling of cells with a SiR-DNA dye (see Fig. 3A,B and Fig. S6A). This approach resembles recent work on morphogen signal recording in gastruloids to distinguish cell sorting from cell signalling (*20*). When initially labelling the T- population (A state) with the dye, cells that were SiR-DNA+, T+ after 24h corresponded to T- cells that activated T (p-transition, see Fig. 3B). Conversely, when initially labelling the T+ population, cells

that were SiR-DNA+, T- after 24h would correspond to T+ cells that turned off T (q-transition, see Fig. 3B). To confirm that the SiR-DNA dye was not affecting the cells, we labelled the T+ and T- populations and did not find any effect on T proportions (see Fig. S6B).

We first mixed 50/50 T+ and T- cells and labelled the latter population with SiR-DNA (Fig. 3C). At 24 hpa, we found that the cells that did not activate T (T-, SiR-DNA+) were enriched on the periphery of the aggregates (see Fig. 3C, upper panel). This was further quantified by computing the radial intensity profile of the difference between the normalised SiR-DNA and T signals (Fig. 3C, lower panel; see Material and Methods). As a control, we mixed SiR-DNA labelled T- and unlabelled T- cells (50/50 ratio) and the enrichment was lost as expected (see Fig. 3C, blue case). Hence, provided that all cells are initially T-, no radial differences in the T population are found during the first 24 hpa. Interestingly, despite radial differences in T expression were found in the 50/50 mixing case, no significant spatial variations in the SiR-DNA signal were detected (Fig. 3C, inset). This result discards the possibility of pure sorting during the first 24 hpa; however, it is not inconsistent with cells simultaneously sorting and changing their fate. Indeed, if one were to assume that T- cells sort to the periphery and T+ cells sort to the core in the 50/50 mixing case, the flux of labelled T- cells that move from the core to the periphery could be balanced by the flux of labelled T- cells that activate from the periphery and move to the core. Radial differences in T expression were consistently found when mixing T+ and T- cells in different proportions (see Figs. 3D, S6 and S7). In particular, when starting with a purely T+ aggregate and labelled with SiR-DNA half of the cells, after 24h the cells that de-activated (T-, SiR-DNA+) were also enriched in the outer region while T+ cells remained enriched in the core (see Figs. S6A and S7 cases $\phi = 1$). This was consistent with our HCR stainings of purely T+ aggregates at 24 hpa (see Fig. S5). Hence, our results show that T- cells are enriched on the periphery of the aggregates irrespective of their previous T expression his-

tory (i.e. both A and C states). We thus conclude that cell sorting and cell fate transitions are likely to occur simultaneously in the aggregates and contribute to the observed spatial differences in T expression. This led us to hypothesise possible differential mechanics between T+ and T- cells leading to mechanical cell sorting.

T+ and T- cell aggregates exhibit differential tissue mechanics

To investigate if the final spatial organisation on T expression was a consequence of differential tissue mechanics, we performed fusion experiments as well as nanoindentation to characterise the tissue mechanical properties (Fig. 4A) (*33, 34*). We found that pairs of T+ cell aggegates fused completely after 10 h while pairs of T- aggregates exhibited a phenomenon known as arrested coalescence, i.e. incomplete fusion (*33*) (Fig. 4B). Interestingly, the dynamics of heterotypic pairs (T+,T-) was clearly different from the homotypic ones (T+,T+ or T-,T-), hinting to the presence of an interfacial tension between tissue types (Fig. 4B, orange curve). We next decided to explore if 24 hpa and 48 hpa gastruloids have similar mechanical properties compared to T- and T+ aggregates, respectively. To do this, we performed the same set of homotypic fusion experiments using 24 hpa and 48 hpa gastruloids. Indeed, similar trends were observed akin to the T- and T+ homotypic fusions, namely 24 hpa pairs exhibited arrested coalescence while 48 hpa pairs fused completely (see Fig. 4C). This is consistent with the timeline of gastruloid differentiation, where T expression is upregulated around 48 hpa. We next performed nanoindentation measurements of the aggregates to measure the effective tissue elasticity (see Material and Methods). By combining the estimate parameters from the fusion experiments and the nanoindentation measurements, we could infer the surface tension γ and viscosity η of the aggregates (*33*). We found a $\sim$ 3-fold increase in surface tension γ and a $\sim$2-fold increase in viscosity η for T+ aggregates compared to T- aggregates (see Fig. 4D, E, F). The effective

elasticity was found to be slightly lower for T+ aggregates compared to T- aggregates (Fig. 4F). While 48 hpa gastruloids showed a similar 3-fold increase in surface tension respect to 24 hpa gastruloids, this was not the case for viscosity which remained similar. We reason that this might be a consequence of the fact that 48h gastruloids have a substantial fraction of T- cells ($\sim$ 50 %, see Fig. 1D) that contribute to a lower tissue viscosity. Overall, our results in Fig. 4 are compatible with the classical picture of tissue sorting, where the higher surface tension tissue stays in the core while the lower surface tension tissue is restricted to the periphery (*18, 35*). Well known candidate proteins driving these different tissue affinities are cadherins (*18, 36, 37*). Indeed, we confirmed such a difference at the protein level using Western blots (see Fig. S8) and found that N-cadherin (Cdh2) levels where higher in T+ aggregates than in T- aggregates. Conversely, E-cadherin (Cdh1) levels where higher in T- than in T+ aggregates. Similarly, RNA expression of the homologous cadherins showed differential expression between pluripotent and primitive streak-like states, giving additional support to this evidence (see Fig. 2E). We thus conclude that differential cadherin levels might be involved in the sorting process, in line with other studies on gastruloids (*38, 39*). In all, we find changes in the material properties of gastruloids from 24 to 48 hpa which are concomitant with the increase in T+ population during this same time period. Our results suggest that T expression modifies the mechanical properties of the tissues leading to cell sorting.

Cell-cell communication explains T proportions in the 3D cellular aggregates

The fact that no spatial variations in the SiR-DNA signal were found in the cell proportion experiments (Fig. 3C, inset) implies that cell sorting is not the only mechanism at play and suggests a key role of cell differentiation during symmetry breaking. We thus asked if cell-cell communication is required to explain T dynamics in the cell proportion experiments in Fig. 1.

We first noticed that the non-monotonous behaviour at 48 hpa in Fig. 1D is incompatible with a simple linear stochastic process (*40, 41*) of autonomous cell fate decisions. This is because such a process leads to a linear dependence of the fraction $\phi(t)$ of T+ cells at a time t on the initial fraction $\phi(0)$ (see Appendix). Hence, we argue that some form of cell-cell communication is necessary to account for the nonlinear dependence on the initial cell populations observed in the experiments. We considered a minimal three-state model (*41–44*) consistent with our analysis of scRNA-seq data (Fig. 5A). We performed a numerical exploration of 24 possible cell signalling models in which states A and B can control differentiation through cellular feedback (see Fig. S9 and Appendix) and found that, in the mean field approximation, the models that best fit the data correspond to the ones where the pluripotent population (state A) inhibits cell differentiation, specifically the B-C transition (see Figs. S9, S10). The previous cell-cell signalling scenario has been considered as a plausible paracrine feedback mechanism, whereby residual pluripotent cells inhibit cell differentiation (*41*). In Fig. 5A,B,C (left) and Fig. S1A we show the model that best fits our experimental data, which considers state A inhibiting both p and q-transitions. From the fit we obtain the transition rates ($p = 0.14 \pm 0.04$ h^{-1}, $q = 0.07 \pm 0.01$ h^{-1}, mean $\pm$ SD) as well as the feedback strength parameter ($K = 0.21 \pm 0.07$, mean $\pm$ SD). Thus, we find that the rate of cell differentiation and cell-cell rearrangements (given by the fusion rate, see Fig. 4B,C) are of the same order, suggesting that biochemical and mechanical cell activites occur simultaneously during symmetry breaking.

We next asked how the parameters in our differentiation model are affected under perturbations of the main signalling pathways involved in symmetry breaking. In agreement with the previously reported role of Wnt/Fgf signalling for Bra/T activation (*13, 29, 45*) our scRNA-seq analysis showed Fgf8 and Wnt3 as highly coexpressed with T and downregulated with pluripotent markers such as Nanog or Sox2 (Fig. 2E). When Fgf signalling was inhibited from 24

hpa to 48 hpa using PDO3, T was downregulated for low $\phi_B(0)$ (Fig. 5B, right). The model predicted that while feedback was retained, transitions from state A to B would be virtually abolished ($q'/p' = 23 \pm 19$, mean $\pm$ SD). By using the inferred parameters from the experiments, we plotted the predicted time evolution of the three states (see Figs. 5C, right). To test the previous theoretical prediction, we considered the case of 50/50 T+/T- starting populations (i.e. $\phi_B(0) = 0.5$). In this case, the model predicts that after 48h, the A-state cells do not transition to state B because of Fgf inhibition, while almost all B cells transition to state C. This was confirmed through HCR stainings where the T (state B) signal was almost absent while Nanog and Aldh1a2, Gata6 signals (states A and C, respectively) where the dominant ones (see Fig. S11). Qualitatively similar results were found on T proportions when inhibiting the Wnt and Nodal/Tgf-β pathways (see Fig. S12). Therefore, we find that Fgf, Wnt and Nodal signals control the p-transition but not the q-transition. Our model shows that cell-cell communication is key to explain the dynamics of the T+ population, which depends on the initial T+ fraction and the strength of the feedback K (see Appendix and Fig. S1A). We thus conclude that the initial T+ population controls the timing of gastruloid development as a consequence of cell-cell communication controlling cell differentiation.

Discussion

In this work, we uncovered that cell-cell communication controls cell differentiation and the timing of symmetry breaking in gastruloids. By systematically varying the amount of T+ cells in the 3D aggregates we found that T dynamics is highly dependent on the initial T+ fraction. This behaviour can be successfully explained through a minimal cell fate model including cell-cell communication. Several important considerations can be drawn from our results. First, our model is consistent with the scaling of cellular populations as observed in gastruloids by

varying their initial size (*29, 30, 46*). Second, despite our model does not account for the spatial distribution of the cellular fates, it provides very good fits to the experimental data. A possible explanation would be that cell signalling occurs over length scales larger than the cell fate patterns that arise during gastruloid formation. Third, gastruloids are not robust to changes in the initial T+ population. This last result is consistent with the variability of the gastruloid system when cells are cultured in ESLIF conditions (*26, 29*), where cellular states are rather heterogeneous compared to 2i-LIF conditions.

Finally, our cell proportion experiments and HCR stainings also reveal spatial differences in T expression between the core and periphery of the aggregates prior to symmetry-breaking, whereby the T+ cells that lose T expression are found on the periphery of gastruloids at 48 hpa. This radial organisation is reminiscent of recent work (*27*) where early spatial variability in pluripotency was observed in gastruloids prior to symmetry-breaking. In this case, primitive streak like cells were found on the periphery and pluripotent-like cells organized in the gastruloid core (*27*). A potential mechanism driving this radial organisation is cell sorting (*18,47–51*). Indeed, our observation that there exist mechanical differences between T+ and T- tissues supports such an idea. Additionally, recent experiments recording morphogen signals have shown that during tissue polarisation in gastruloids single-cell Wnt activity predicts future cellular position and that axis symmetry breaking is most likely a consequence of sorting rearrangements involving cell adhesion differences (*39*).

Our study suggests that not only cell-cell rearrangements, but also cell-cell communication, are likely to work synergistically during symmetry breaking in gastruloids. One possible explanation is that cell signalling controls cellular proportions independently of the size of the aggregates, while differential mechanics drives the spatial organisation of the cellular fates. Most

importantly, our work shows that the timescale of cell-cell rearrangements ($R\eta/\gamma$) and the typical timescale of cell fate transitions ($1/p$) are similar and found to be on the order of ~ 10 h. Hence we argue that both biochemical and mechanical processes evolve under a common morphogenetic timescale in the system. Understanding how multicellular systems integrate both biochemical and mechanical activities to ensure robust self-organisation will help us advance in the principles of biological self-organisation.

Material and Methods

Transgenic mESC cell line maintanence

Bra/T::GFP mouse embryonic stem cells (*52*) were maintained in ESLIF medium, consisting of KnockOut Dulbecco's Modified Eagle Medium (DMEM) supplemented with 10% fetal bovine serum (FBS), 1x Non-essential aminoacids (NEEA), 50 U/mL Pen/Strep, 1x GlutaMax, 1x Sodium Pyruvate, 50 μM 2-Mercaptoethanol and leukemia inhibitory factor (LIF). Cells adhered to 0.1% gelatin-coated (Millipore, ES-006-B) tissue culture-treated 25 cm^2 or 75 cm^2 flasks (T25 Corning 353108; T75 Corning, 353136) in an incubator at 37 °C and 5% CO_2. Under these conditions, the percentage of T+ cells varied from 1 to 5% of the total population as determined by FACS.

Cell proportion experiments

Cells were cultured in two T75 culture flasks to a confluency of $\sim 50 - 80\%$. For the case of exogenous labelling, in the same day of FACS sorting, both flasks were washed with 15 mL $PBS^{+/+}$ and one of them was incubated with 12 mL NDiff227 media (N2B27) (Takara Bio, #Y40002) containing 1.6 μM SiR-DNA (Spirochrome, SC007) for 1h while the other was incubated with N2B27 only. Four different conditions were obtained: (1) T-, SiR-DNA+, (2) T-, (3) T+, SiR-DNA+ and (4), T+ in 2 mL Eppendorf tubes containing 1.2 mL N2B27. Subsequently, cells were mixed in different proportions and seeded in 96-well U-bottom plates (Greiner Cellstar, #650970) (375 cells per well). 96-well plates of mES cell aggregates were imaged using a PerkinElmer Opera Phenix® system using a x20 dry objective and N.A. 0.4 in confocal mode. A z-stack was acquired for every aggregate at 4 μm intervals.

In situ hybidization chain reaction

Gastruloids were harvested from round bottom 96-well plates and transferred to 1.5 mL Eppendorf tubes with wide-bore p200 RNAase free tips. N2B27 media was removed after 3 washes for 5 min each with 1ml DPBS$^{-/-}$ and then samples were fixed with cold 4% PFA in DPBS$^{-/-}$ and kept at 4°C overnight. The following day, PFA was removed from the samples by washing 3x 1mL DPBS$^{-/-}$. At this point the samples were kept at 4° up to a week. Next, the samples were dehydrdated and permeabilized with a series of 1 mL 100 % methanol (MeOH) washes (x4 10 min washes and x1 50 min wash at RT). The samples were rehydrated with a series of graded 1 mL MeOH/PBST (PBST: 1X PBS, 0.1% Tween 20) washes for 5 min each at RT (75/25, 50/50, 25/75, 5x 100/0). For the detection stage, a pre-hybridization step was done by adding 500 μL of probe hybridization buffer (PHB, Molecular Instruments) to the sample for 30 min at 37 °C. The probe solution was prepared by adding 0.4 pmol of each detection probe mixture to 500 μL of PHB. The pre-hybridization solution was removed and the probe solution was added and incubated overnight at 37°C. The next day the excess detection probes were removed by washing x4, 15 min with 500 μL probe was buffer (PWB, Molecular Instruments) which was pre-heated at 37°C. Next, the samples were washed twice for 5 min with 5 x SSCT (5x Sodium chloride sodium citrate, 0.1% Tween in water) at RT. For the amplification stage, a pre-amplification step was done by adding 500 μL of amplification buffer (Molecular Instruments) equilibrated at RT for 30 min. Next, 6 pmol of hairpins h1 and h2 1:1 were prepared by snap cooling 2 μL from a 3 μM stock (heated at 95°C for 90 s and cooled down to RT in the dark for 30 min). The hairpin mixture was prepared by diluting snap-cooled h1 and h2 hairpins to 1:250 in amplification buffer at RT. The amplification solution was removed from the sample and 250 μL of the hairpin mixture were added to each reaction to a final concentration of 12 nM for each hairpin. The samples were incubated at RT overnight. Finally, on the next day the excess hairpins were removed by washing with 500 μL 5x SSCT at RT (2 x 5 min, 2 x 30 min,

1 x 5 min). Samples were stored at 4°C protected from light before microscopy. Gastruloids were transferred to flat-bottom 96 well plates (PerkinElmer Cell Carrier - 96 Ultra) and were imaged using a PerkinElmer Opera Phenix® system using a x20 water and N.A. 1 in confocal mode. A z-stack was acquired for every aggregate at 4 μm intervals.

Cell lysis and Western blots

600-cell gastruloids were pulled together at 24 hpa from a 96-well plate ($\sim 6 \cdot 10^4$ cells). Gastruloids were treated with 0.05 % Trypsin-EDTA (Thermo Fisch der Scientific) for 3 min. The cell suspension was washed with 5 mL DPBS$^{+/+}$ and spun down for 3 min at 900 rpm twice to remove the excess Trypsin. Cells were washed twice with 5 mL ice-cold TBS-Ca^{++} buffer (5 mM $CaCl_2$, 50 mM TrisHCl pH 7.5, 150 mM NaCl) containing 1 mM PMSF in DMSO and spun down for 3 min at 900 rpm. Cells were subsequently washed with 5 mL ice-cold HBSS. Finally, 250 μL RIPA lysis buffer (500 mM TrisHCl pH 7.5, 10 mM EDTA, 1.5 M NaCl, 10 % v/v Np40 and 2.5 % m/v DOC) containing one tablet of protein inhibitor cocktail diluted 1:7 was added to the cell lysate and the cells were kept on ice for 15 min. The lysate was transferred into a micro-centrifuge tube and was shaken for 1h at 48°C. Finally, the lysate was passed through a Qia shredder and centrifuged at 15000 rpm) at 48°C for 15 min. At this point the lysate was flash frozen and stored at -20°C. To perform the Western blots, cell lysates were resolved on SDS-polyacrylamide gels (BIO-RAD Mini-Protean Precast Gels) and the proteins transferred onto nitrocellulose blotting membranes (Amersham). Membranes were blocked for 30 min at room temperature (RT) with 10 % (w/v) skimmed milk diluted in TBS (10 mM Tris-HCl [pH 7.4] and 100 mM NaCl)-0.1% Tween-20 (TBS-T), and then probed for overnight at 4°C with primary antibodies diluted in 5% skimmed milk in TBS-T. After several washes, the membranes were incubated at RT for 45 min with horseradish peroxidase-conjugated secondary antibodies (Invitrogen) diluted in 5% skimmed milk in TBS-T. Antibody

binding was detected by chemiluminiscence (ECL Prime Western Blotting Detection Reagent, Amersham) on a Fusion Fx Spectra Imager (Vilber). The antibodies used can be found in Table S2.

Image analysis

Image analysis was done using the software MOrgAna (*53*). In order to obtain the image masks, a custom-made Python scripts for downstream data processing were used. For the cell proportion experiments, average intensities were computed at the focal plane and the background signal was subtracted. For the radial analysis, we first pre-processed the sirDNA signal I_{sirDNA} for each aggregate by removing high intensity peaks corresponding to 0.3% of the total signal. Next, the relative intensity measure $\delta I = I_{\mathrm{sirDNA}}/\langle I_{\mathrm{sirDNA}}\rangle - I_{\mathrm{GFP}}/\langle I_{\mathrm{GFP}}\rangle$ was computed for each aggregate image, where the spatial average $\langle \ldots \rangle$ was performed in the masked region. The relative intensity radial profiles for each aggregate were obtained by counting the values δI in a set of pixels at a distance r from the center of mass of the aggregate and normalising by this value. Finally, in order to average the profiles over different aggregates, we first normalised the radial axis by interpolating the profiles. For the morphometric quantification of gastruloids, the software MOrgAna was used to straighten the gastruloids (see Ref. (*53*) for details) and the aspect ratio was defined as the ratio between the major axis L and minor axis d (see Fig. 1E and S1B). In order to quantify gastruloid polarisation, the averaged anteroposterior intensity profile $I(x)$ was obtained by analysing several gastruloids using the software, where x was the normalised anteroposterior axis such that $x \in [0, 1]$. Finally, the polarisation parameter P was defined as $P(x) = \int_0^1 I(x)(x - 1/2)dx / \int_0^1 I(x)$.

Nanoindentation and inference of mechanical parameters

The mechanical measurements were done using the Chiaro Nanoindenter (Optics11) adapted to a Leica DMi8 inverted microscope. The aggregates were transferred from the multiwell plates to μ-Slide 8 well coverslips (ibidi, #80826) coated with 0.1 % gelatin and containing warm N2B27. Indentations were done with a spherical cantilever probe of 27 ± 3 μm of radius and a stiffness of 0.025 ± 0.002 N m^{-1}. The approach speed was 5 μm s^{-1} and the indentation depth was $\simeq 6$ μm (~ 3 % of the typical size of an aggregate). The effective elastic modulus E_{eff} was calculated by fitting the Hertz's model to the indentation curves and the corresponding shear modulus was obtained as $\mu = (E_{\text{eff}}/2)(1-\nu^2)/(1+\nu)$, assuming a Poisson's ratio of $\nu = 1/2$. The average effective elastic modulus was obtained by averaging over the different aggregates. In order to obtain the effective surface tension γ and viscosity η of the cellular aggregates, the viscocapillary velocity γ/η and the elastocapillary length γ/μ were obtained by fitting a Kelvin-Voigt model to the fusion experiments in Fig. 4B,C as explained in Refs. (*33, 34*). Finally, by using the obtained value of the shear elastic modulus μ from the nanoindentation measurements, the parameters η and γ were inferred.

Cell fate model exploration and inference of cell fate transition rates

The experimental dataset (24, 48 and 72 hpa data) was fit to the model using 4 parameters, $\alpha = q/p$, K, τ_{24} and τ_{48}, where the last parameters correspond to the dimensionless timepoints at 24 hpa and 48 hpa. The reason why four parameters are needed instead of three (p, q, K) is because the seeding time ($\tau = 0$) does not correspond to the time when signalling starts. Hence, an additional time parameter is needed. The timescale of the process was then obtained as $24\,\text{h}/(\tau_{48} - \tau_{24})$. The dimensionless timepoint at 72 hpa was obtained as $\tau_{72} = 2\tau_{48} - \tau_{24}$. For the model exploration in Fig. S9 and S10, stochastic simulations were performed to find estimations of the mean values of $\phi_B(t)$ for all the master equations. The main reason being

that in general not all 24 models had a closed solution for $\phi_B(t)$ as in Eq. S16. Each model was simulated with $N = 10^4$ individual realisations starting from 5 different proportions of A and B states to compute the mean values. The previous system size provided a stable enough estimation of the mean values. The four parameters were fit using the NOMAD algorithm (*54*). We defined the loss term for the optimisation as the absolute error between the mean value per time point of the data and the means of the simulation. The exploration space for the parameters was $\alpha \in (0, 10), K \in (0, 10), \tau_{24} \in (0, 100), \tau_{48} \in (0, 100)$. The experimental data in Figs. 1 and S1A were fit to the cell-cell communication model where state A inhibits both AB and BC transitions (see Appendix Eqs. S15 and S16). This was done using `curve_fit` function from `scipy.optimize` in Python.

Single-cell RNA sequencing analysis

The 24 and 48 hpa scRNA sequencing data was used from previous work in Ref. (*29*). Next, we detail the different steps of the analysis:

Quality control, normalisation and scaling. We analysed each sample independently corresponding to a time point each. We calculated the standard quality control metrics of total counts per cell, number of expressed genes per cell, and mitochondrial fraction. We heuristically set quality control thresholds for each metric based on the observed bimodalities of the histogram plots. Cells outside the thresholds were removed from further analysis. In the following, we used scrublet algorithm (*55*) to impute candidate doublets. We estimated the scrublet score threshold using the heuristic method described in the original paper, by observing the bimodality on the histogram of simulated doublets scrublet scores. Cells with scores above this threshold were imputed as doublets and removed from further analysis. The remaining cells in the count matrix were normalised to a total count sum of 10^5 counts. The analysis was insensi-

tive to the specific choice of this parameter. In addition, the matrix was log-one-plus normalised before downstream analysis.

Feature selection, dimensionality reduction and visualisation. For dimensionality reduction genes were selected using the `scanpy.pp.highly_variable_genes` function with "seurat" flavor (*56*) and the top 2000 genes were used as input dimensions for a Principal Component Analysis (PCA). The results were insensitive to the specific number of top genes selected. With the PCA, we retained the 20 components with more explained variance. This choice was based on the selection of components by perfoming a randomisation test such that all datasets have the same number of components. The selection of components was also orientative and robust to the specific choice on the number of components. With the selected number of principal components, we generated a k-nearest neighbours (k-NN) graph representation of the data using the `scanpy.pp.neighbors` with correlation metric. UMAP plots were created for visualisation using the `scanpy.tl.umap` function with default parameters.

Annotation. For annotation, we used the marker genes appearing in Table S1. The custom annotation algorithm worked in two steps. First, cells that had at least one count of a marker gene were considered positive for the gene and negative only if there were no counts present. Each cell was assigned a fate if it expressed the combination of positive or negative markers for that specific fate. Cells that were annotated with more than one fate were treated as "Multi-assigned", and cells with no annotation as "Unassigned". In a second step, we trained a k-NN classifier over the PCA space with the uniquely assigned cells as the training set and the "Multi-assigned" and "Unassigned" cell as prediction cells. These two sets of cells were annotated using the majority vote of the remaining k-NN 15 nearest neighbours.

Time sample integration. For integrating the time samples of each dataset we combined the samples after the quality control step. With this matrix, we normalised, scaled, selected features and performed the PCA analysis in the same procedure described above. With the retained

PCA components, we used the `scanpy.external.pp.harmony` function to correct for the batch effect between samples. The corrected representation was then used for constructing the graphs, the UMAPs, clustering and annotation as described before.

Code availability

All scRNA-seq analysis was performed in Python. The scripts can be found in github (https://github.com/dsb-lab/gastruloids_positive_feedback_scRNAseq_analysis). To mantain reproducibility, we performed the analysis using a docker image containing all the required software to reproduce the analysis, provided in Dockerhub (https://hub.docker.com/r/dsblab/single_cell_analysis), and using the v0.6 image. Fitting of the mean field model was performed using Julia. The scripts can be found in github (https://github.com/dsb-lab/gastruloids_positive_feedback_mean_field_fitting).

Acknowledgments

We thank S. Gsell, P.-F. Lenne, A. Martinez Arias, V. Ruprecht, J. Sharpe, K. Stapornwongkul and V. Weichselberger for critical reading of the manuscript. We thank the Mesoscopic Imaging Facility (EMBL Barcelona) for assistance with imaging and the Tissue Engineering Unit (CRG). We thank all the members of the Trivedi group for feedback on the project. D.O. acknowledges funding from Juan de la Cierva Incorporación with Project no. IJC2018-035298-I, from the Spanish Ministry of Science, Innovation and Universities (MCIU/AEI). This work was supported by the Spanish Ministry of Science and Innovation and FEDER, under projects FIS2017- 92551-EXP and PID2021-127311NB-I00, by the "Maria de Maeztu" Program for Units of Excellence in R&D (grant CEX2018-000792-M), and by the Generalitat de Catalunya (ICREA Academia program). G. T-C. was supported by an FPU doctoral fellowship from the Spanish Ministry of Education and Universities (reference FPU18/05091).

Author contributions

Conceived and designed the experiments: D.O., V.T. Performed the experiments: D.O., Kr.A., D.F.-M., E.H., Ke.A. Analyzed the data: D.O., G.T.-C., J.G.-O. Contributed materials/analysis tools: D.O., G.T.-C., J.G.-O., V.T. Wrote the paper: D.O., G.T.-C., V.T.

Main Figures

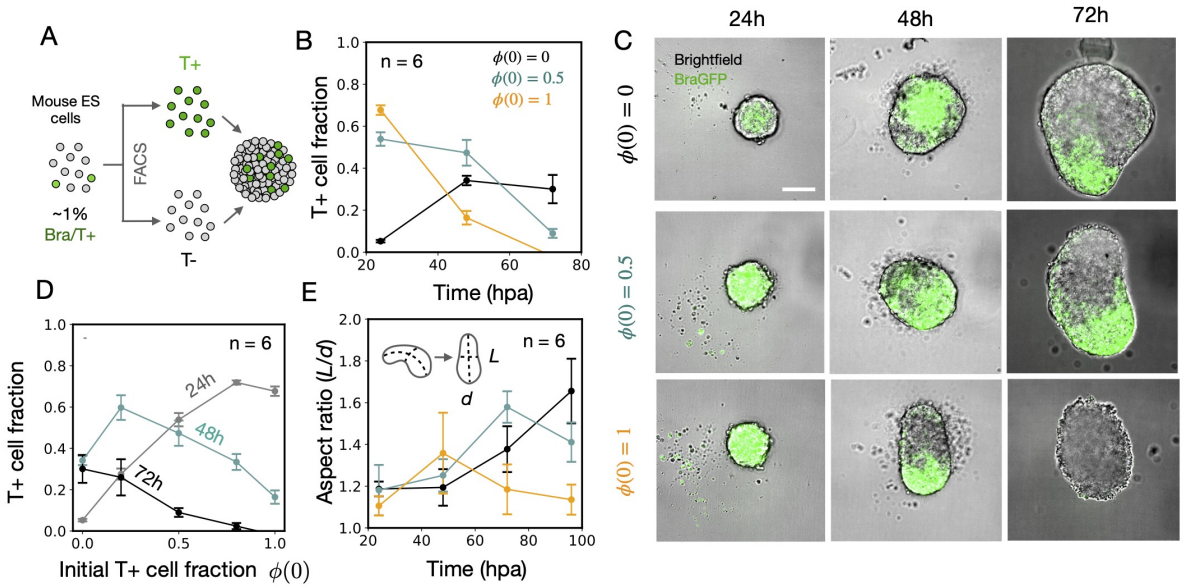

Figure 1: **T dynamics under controlled cell proportions.** A) Schematics of the cell proportion experiments. mESCs were cultured in 2D under ESLIF conditions, and were subsequently FACS sorted into T+ and T- populations. The different cell populations were mixed in different proportions to form 3D aggregates in multi-well 96 plates in N2B27 medium. B) Time evolution of the T+ fraction for different starting T+ populations $\phi(0) = 0, 0.5, 1$. C) Representative brightfield images of the aggregates at 24, 48 and 72 hpa for initial T+ fractions $\phi(0) = 0, 0.5, 1$. The images are composed with the signal from a GFP reporter of T expression. Scale bar: 200 μm. D) T+ cell fraction as a function of the initial fraction of T+ cells ϕ for 24, 48 and 72 hpa. In each experiment $\simeq 50$ cell aggregates were analysed. The fraction of T+ cells was obtained by normalizing the GFP intensity by the extrapolated intensity at $\phi = 1$ at 24 hpa. E) Time evolution of the aspect ratio of gastruloids for initial T+ fractions $\phi(0) = 0, 0.5, 1$. Error bars in panels B and D correspond to $2 \times$ SEM over $n = 6$ replicates. In each replicate ~ 10 aggregates were averaged for each condition. Error bars in E indicate SD.

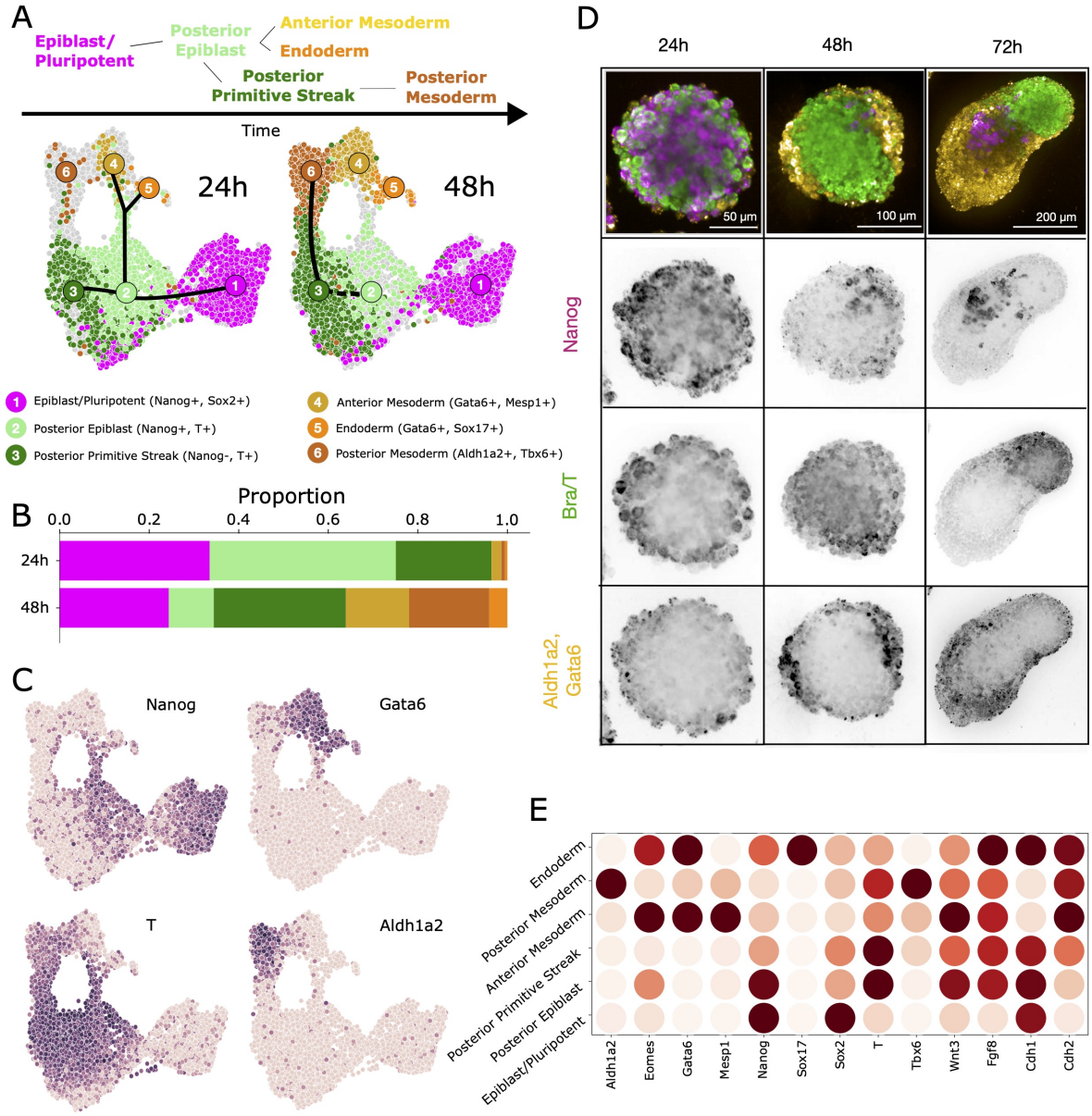

Figure 2: **Cell fate dynamics during early gastruloid differentiation**. A) Integrated UMAP of 24 hpa and 48 hpa (light gray) and 24 hpa, 48 hpa data (colored) showing how the different states are populated over time. B) The corresponding proportions by annotation are shown. C) UMAPs of different relevant genes are shown. D) HCR stainings for the 3 main cellular states at 24, 48 and 72 hpa: Nanog+ pluripotent state, a T+ primitive streak-like state and further differentiated states being Aldh1a2+ and Gata6+. E) Mean normalised and log-normalised gene expression per cluster of relevant genes per annotation cluster at 48 hpa.

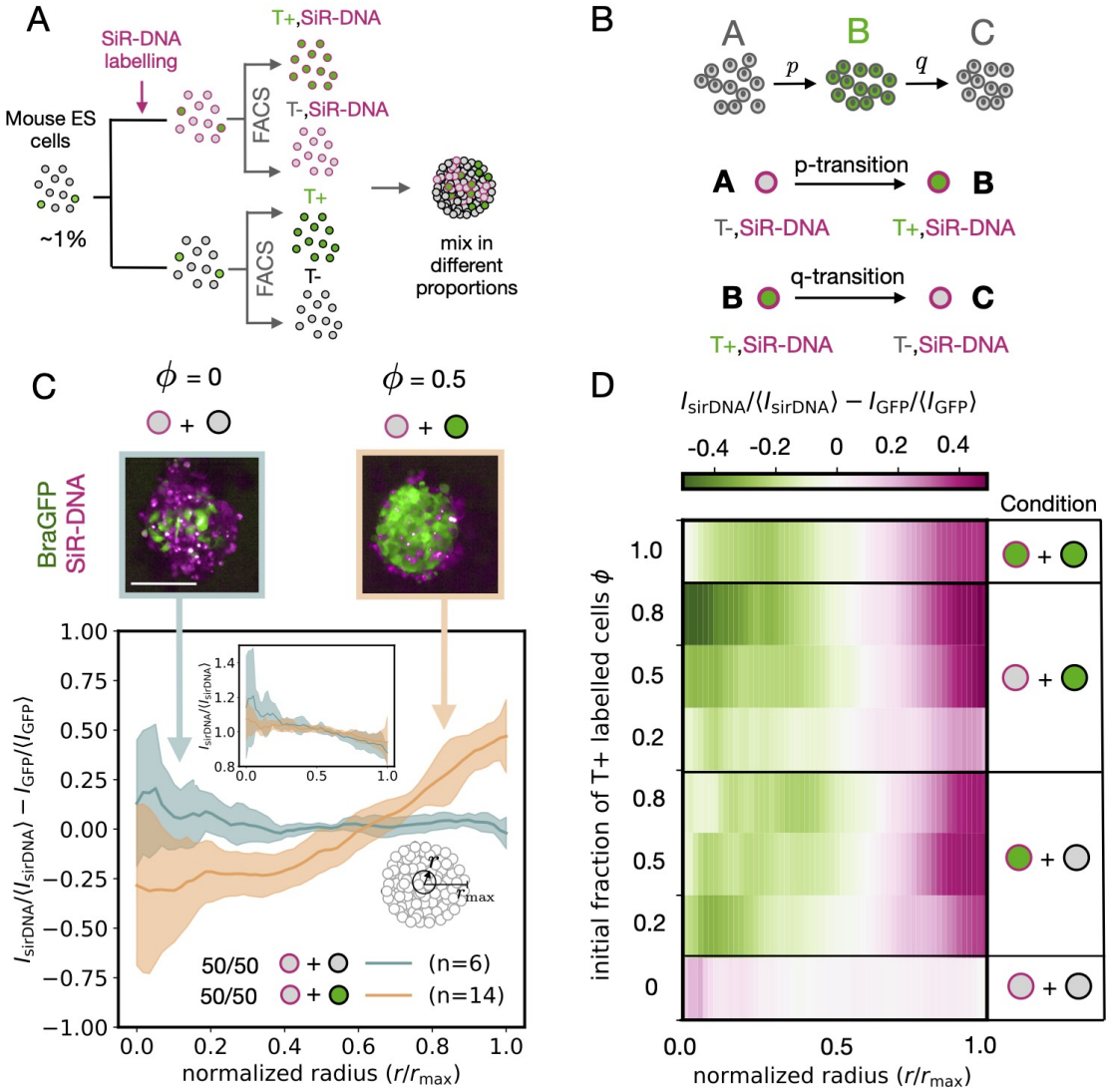

Figure 3: **Spatial organisation of T in cell proportion experiments** A) Schematics of the cell proportions experiment with exogenous labelling. mESC were cultured in 2D under ESLIF conditions and a certain fraction was labelled with SiR-DNA for 1h. Cells were subsequently FACS sorted into four different populations: (1) T+, SiR-DNA+; (2) T-, SiR-DNA+; (3) T+,SiR-DNA- and (4) T-,SiR-DNA-. Finally, the different cell populations were mixed in different proportions to form 3D aggregates in multi-well 96 plates in N2B27 medium and studied at 24 hpa. B) SiR-DNA labelling of the T- cells allowed us to detect p-transitions while labelling of T+ cells allowed us to detect q-transitions. C) Cell proportion experiments mixing 50/50 populations of labelled and unlabelled cells. When the cell populations are different, T- cells are enriched on the surface of the aggregate. Radial intensity profile showing the enrichment of GFP signal on the inside of the aggregate compared to the SiR-DNA signal. Inset: Radial SiR-DNA signal profile showing no significant spatial organisation. Images correspond to confocal maximum intensity projections at 24 hpa. Shaded error bars correspond to SD. D) Colormaps of the radial profile for different starting fractions of T+ cells ϕ as well as different populations labelled with SiR-DNA. In the inner part of the aggregate the majority of cells are in state B, while in the periphery the majority of cells are in either A or C states.

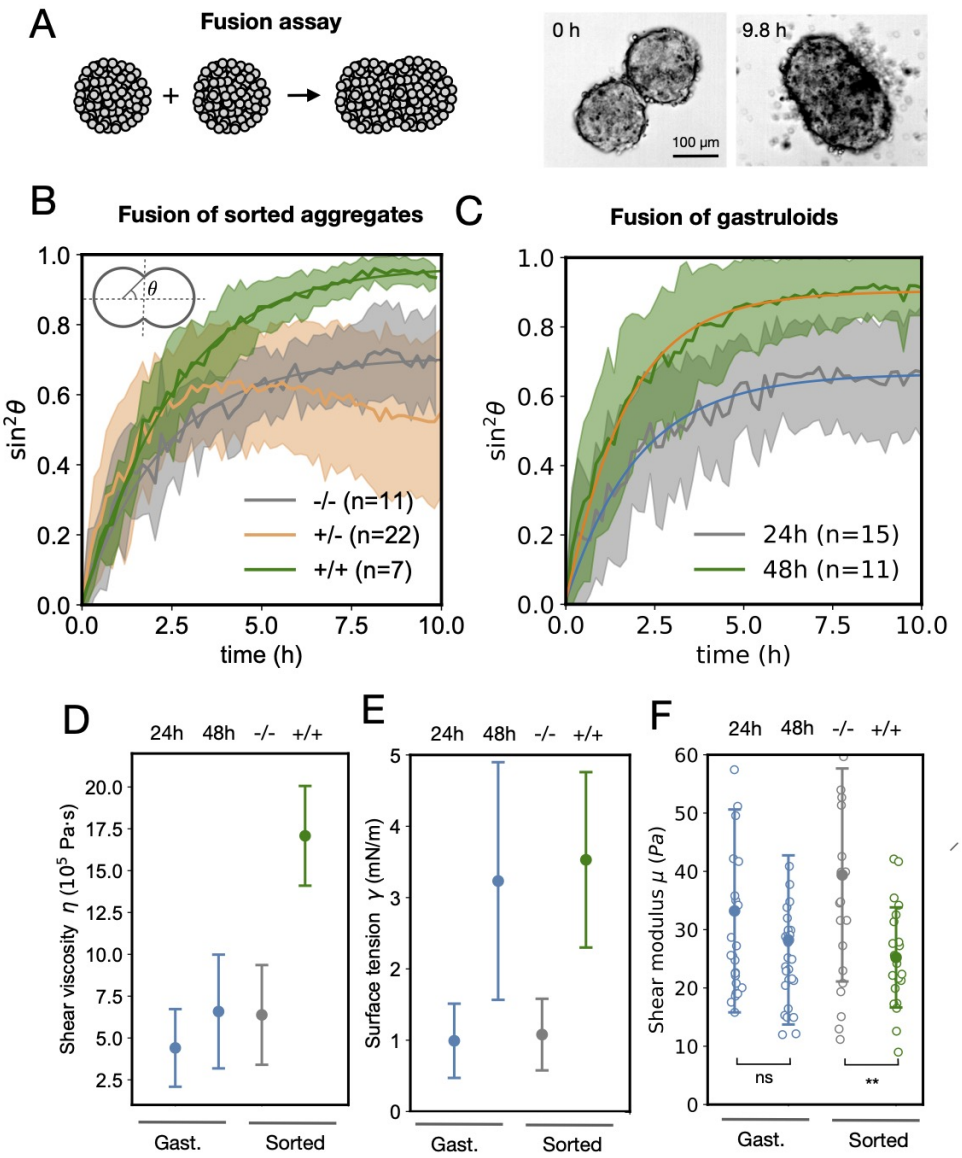

Figure 4: **T expression impacts the mechanics of cellular aggregates** A) Fusion assay. Brightfield images of two fusing T- sorted aggregates before and after fusion. B) Time evolution of $\sin^2\theta$, where θ corresponds to the contact angle between the two aggregates (see inset). The average curves correspond to homotypic (T+/T+, T-/T-) and heterotypic (T+/T-) fusions of T+ and T- sorted aggregates.The average radius of T- and T+ aggregates was 80 $\pm$ 6 μm and 88 $\pm$ 6 μm, respectively (mean $\pm$ SD). n corresponds the number of analyzed aggregates per condition. C) Time evolution of $\sin^2\theta$ for the fusion of 24 hpa and 48 hpa gastruloids. The average radius of 24 hpa and 48 hpa gastruloids was $R = 100 \pm 7$ μm and $R = 145 \pm 11$ μm, respectively (mean $\pm$ SD). Solid lines correspond to fits to a mathematical model considering the aggregates behave as Kelvin-Voigt materials. D, E) Inferred effective tissue shear viscosity η and surface tension γ for gastruloids, T+ and T- aggregates. F) Nanoindentation measurements of the shear elastic modulus μ for gastruloids, T+ and T- aggregates. ** $P < 0.01$, both t-test and Mann-Whitney U test. ns: both t-test and Mann-Whitney U test. Shaded error bars correspond to SD.

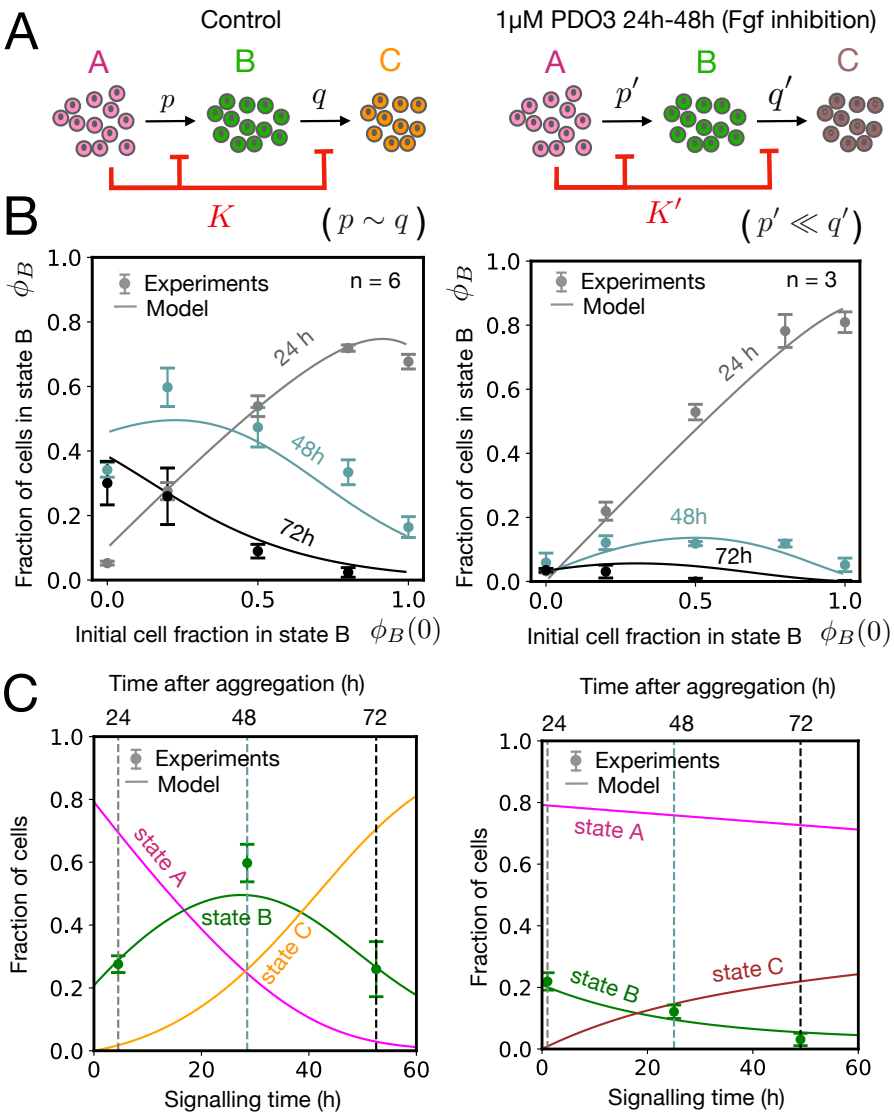

Figure 5: **Cell-cell communication explains cell fate dynamics in gastruloids**. A) Minimal cell-cell signalling model considering cells transition through 3 main cellular states (A, B and C). State A is assumed to prevent cell differentiation from A to B and from B to C with feedback strength K. In principle, given that the inhibitory signals might affect cell differentiation, we denote state C with a different color (brown). B) Evolution of the fraction of cells in state B as a function of the initial fraction of cells in state B for 24, 48 and 72 hpa. The fraction of cells in state B was obtained by normalizing the GFP intensity by the extrapolated intensity at $\phi_B = 1$ at 24 hpa. Solid lines correspond to the fits using the models in panel A (see Appendix). The fitted parameters for the control case (left) are $q/p = 0.5 \pm 0.1$ and $K = 0.21 \pm 0.07$ (mean $\pm$ SD). For the inhibited case, the fitted parameters are $q'/p' = 23 \pm 19$ and $K' = 0.3 \pm 0.2$. Error bars correspond to $2 \times$ SEM over different replicates without the addition of SiR-DNA. In each replicate ~ 10 aggregates were averaged for each condition. C) Time evolution of the three states considering $\phi_A(0) = 0.8$, $\phi_B(0) = 0.2$, $\phi_C(0) = 0$ and using the fitted parameters from the experiments (see Material and Methods). Vertical dashed lines indicate 24, 48 and 72 hpa while the x-axis corresponds to the signalling time. The initial timepoint $t = 0$ is inferred from the fit (see Material and Methods).

References

1. Christian P Petersen and Peter W Reddien. Wnt signaling and the polarity of the primary body axis. *Cell*, 139(6):1056–1068, 2009.

2. Kyle M Loh, Renée van Amerongen, and Roel Nusse. Generating cellular diversity and spatial form: Wnt signaling and the evolution of multicellular animals. *Developmental cell*, 38(6):643–655, 2016.

3. Christiane Nüsslein-Volhard and Eric Wieschaus. Mutations affecting segment number and polarity in drosophila. *Nature*, 287(5785):795–801, 1980.

4. Toshiro Mizuno, Etsuro Yamaha, Atsushi Kuroiwa, and Hiroyuki Takeda. Removal of vegetal yolk causes dorsal deficencies and impairs dorsal-inducing ability of the yolk cell in zebrafish. *Mechanisms of development*, 81(1-2):51–63, 1999.

5. S-R Chen and David Kimelman. The role of the yolk syncytial layer in germ layer patterning in zebrafish. *Development*, 127(21):4681–4689, 2000.

6. W Ross Waldrip, Elizabeth K Bikoff, Pamela A Hoodless, Jeffrey L Wrana, and Elizabeth J Robertson. Smad2 signaling in extraembryonic tissues determines anterior-posterior polarity of the early mouse embryo. *Cell*, 92(6):797–808, 1998.

7. Nikolas Uez, Heiko Lickert, Jürgen Kohlhase, Martin Hrabe de Angelis, Ralf Kühn, Wolfgang Wurst, and Thomas Floss. Sall4 isoforms act during proximal–distal and anterior–posterior axis formation in the mouse embryo. *Genesis*, 46(9):463–477, 2008.

8. Keisuke Ishihara and Elly M Tanaka. Spontaneous symmetry breaking and pattern formation of organoids. *Current Opinion in Systems Biology*, 11:123–128, 2018.

9. Nozomu Takata, Eriko Sakakura, Mototsugu Eiraku, Takeya Kasukawa, and Yoshiki Sasai. Self-patterning of rostral-caudal neuroectoderm requires dual role of fgf signaling for localized wnt antagonism. *Nature communications*, 8(1):1–16, 2017.

10. Derk ten Berge, Wouter Koole, Christophe Fuerer, Matt Fish, Elif Eroglu, and Roel Nusse. Wnt signaling mediates self-organization and axis formation in embryoid bodies. *Cell stem cell*, 3(5):508–518, 2008.

11. Susanne C Van den Brink, Peter Baillie-Johnson, Tina Balayo, Anna-Katerina Hadjantonakis, Sonja Nowotschin, David A Turner, and Alfonso Martinez Arias. Symmetry breaking, germ layer specification and axial organisation in aggregates of mouse embryonic stem cells. *Development*, 141(22):4231–4242, 2014.

12. Andrea Meinhardt, Dominic Eberle, Akira Tazaki, Adrian Ranga, Marco Niesche, Michaela Wilsch-Bräuninger, Agnieszka Stec, Gabriele Schackert, Matthias Lutolf, and Elly M Tanaka. 3d reconstitution of the patterned neural tube from embryonic stem cells. *Stem cell reports*, 3(6):987–999, 2014.

13. David A Turner, Mehmet Girgin, Luz Alonso-Crisostomo, Vikas Trivedi, Peter Baillie-Johnson, Cherise R Glodowski, Penelope C Hayward, Jérôme Collignon, Carsten Gustavsen, Palle Serup, et al. Anteroposterior polarity and elongation in the absence of extra-embryonic tissues and of spatially localised signalling in gastruloids: mammalian embryonic organoids. *Development*, 144(21):3894–3906, 2017.

14. Leonardo Beccari, Naomi Moris, Mehmet Girgin, David A Turner, Peter Baillie-Johnson, Anne-Catherine Cossy, Matthias P Lutolf, Denis Duboule, and Alfonso Martinez Arias. Multi-axial self-organization properties of mouse embryonic stem cells into gastruloids. *Nature*, 562(7726):272, 2018.

15. Naomi Moris, Kerim Anlas, Susanne C van den Brink, Anna Alemany, Julia Schröder, Sabitri Ghimire, Tina Balayo, Alexander van Oudenaarden, and Alfonso Martinez Arias. An in vitro model of early anteroposterior organization during human development. *Nature*, 582(7812):410–415, 2020.

16. Alan Mathison Turing. The chemical basis of morphogenesis. *Bulletin of mathematical biology*, 52(1-2):153–197, 1990.

17. Simon Gsell, Sham Leilah Tlili, Matthias Merkel, and Pierre-François Lenne. Marangoni-like tissue flows enhance symmetry breaking of embryonic organoids. *bioRxiv*, pages 2023–09, 2023.

18. Ramsey A Foty and Malcolm S Steinberg. The differential adhesion hypothesis: a direct evaluation. *Developmental biology*, 278(1):255–263, 2005.

19. Malcolm S Steinberg. Differential adhesion in morphogenesis: a modern view. *Current opinion in genetics & development*, 17(4):281–286, 2007.

20. Harold M McNamara, Sabrina C Solley, Britt Adamson, Michelle M Chan, and Jared E Toettcher. Recording morphogen signals reveals mechanisms underlying gastruloid symmetry breaking. *Nature Cell Biology*, pages 1–13, 2024.

21. Christian Schröter, Pau Rué, Jonathan Peter Mackenzie, and Alfonso Martinez Arias. Fgf/mapk signaling sets the switching threshold of a bistable circuit controlling cell fate decisions in embryonic stem cells. *Development*, 142(24):4205–4216, 2015.

22. Dhruv Raina, Azra Bahadori, Angel Stanoev, Michelle Protzek, Aneta Koseska, and Christian Schröter. Cell-cell communication through fgf4 generates and maintains robust proportions of differentiated cell types in embryonic stem cells. *Development*, 148(21):dev199926, 2021.

23. M Sáez, J Briscoe, and David A Rand. Dynamical landscapes of cell fate decisions. *Interface focus*, 12(4):20220002, 2022.

24. Meritxell Sáez, Robert Blassberg, Elena Camacho-Aguilar, Eric D Siggia, David A Rand, and James Briscoe. Statistically derived geometrical landscapes capture principles of decision-making dynamics during cell fate transitions. *Cell Systems*, 13(1):12–28, 2022.

25. Kerim Anlas, Peter Baillie-Benson, Krisztina Arató, David A Turner, and Vikas Trivedi. Gastruloids: embryonic organoids from mouse embryonic stem cells to study patterning and development in early mammalian embryos. *Programmed Morphogenesis: Methods and Protocols*, pages 131–147, 2021.

26. Leah U Rosen, L Carine Stapel, Ricard Argelaguet, Charlie George Barker, Andrian Yang, Wolf Reik, and John C Marioni. Inter-gastruloid heterogeneity revealed by single cell transcriptomics time course: implications for organoid based perturbation studies. *bioRxiv*, pages 2022–09, 2022.

27. Simon Suppinger, Marietta Zinner, Nadim Aizarani, Ilya Lukonin, Raphael Ortiz, Chiara Azzi, Michael B Stadler, Stefano Vianello, Giovanni Palla, Hubertus Kohler, et al. Multimodal characterization of murine gastruloid development. *Cell Stem Cell*, 30(6):867–884, 2023.

28. Lara Avni, Naama Farag, Binita Ghosh, and Iftach Nachman. Gastruloid optimization. *Emerging Topics in Life Sciences*, 7(4):409–415, 2023.

29. Kerim Anlaş, Nicola Gritti, Fumio Nakaki, Laura Salamó Palau, Sham Leilah Tlili, David Oriola, Krisztina Arató, Jia Le Lim, James Sharpe, and Vikas Trivedi. Early autonomous patterning of the anteroposterior axis in gastruloids. *Development*, 151(22), 2024.

30. Kristina S Stapornwongkul, Elisa Maria Hahn, Laura Salamo Palau, Krisztina Arato, Nicola Gritti, Kerim Anlas, Patryk Polinski, Mireia Lopez, Miki Ebisuya, and Vikas Trivedi. Metabolic control of germ layer proportions through regulation of nodal and wnt signalling. *bioRxiv*, pages 2023–12, 2023.

31. Jimmy Tsz Hang Lee and Martin Hemberg. Supervised clustering for single-cell analysis. *Nature methods*, 16(10):965–966, 2019.

32. Sebastian J Arnold and Elizabeth J Robertson. Making a commitment: cell lineage allocation and axis patterning in the early mouse embryo. *Nature reviews Molecular cell biology*, 10(2):91–103, 2009.

33. David Oriola, Miquel Marin-Riera, Kerim Anlaş, Nicola Gritti, Marina Sanaki-Matsumiya, Germaine Aalderink, Miki Ebisuya, James Sharpe, and Vikas Trivedi. Arrested coalescence of multicellular aggregates. *Soft Matter*, 18:3771–3780, 2022.

34. Sotiris Samatas, Martí Planasdemunt-Hospital, and David Oriola. Arrested coalescence: A tool to explore tissue rheology. *Biophysica*, 4(4):604–618, 2024.

35. Malcolm S Steinberg. Adhesion-guided multicellular assembly: a commentary upon the postulates, real and imagined, of the differential adhesion hypothesis, with special attention to computer simulations of cell sorting. *Journal of theoretical biology*, 55(2):431–443, 1975.

36. Jennifer M Halbleib and W James Nelson. Cadherins in development: cell adhesion, sorting, and tissue morphogenesis. *Genes & development*, 20(23):3199–3214, 2006.

37. Akinao Nose, Akira Nagafuchi, and Masatoshi Takeichi. Expressed recombinant cadherins mediate cell sorting in model systems. *Cell*, 54(7):993–1001, 1988.

38. Ali Hashmi, Sham Tlili, Pierre Perrin, Molly Lowndes, Hanna Peradziryi, Joshua M Brickman, Alfonso Martínez Arias, and Pierre-François Lenne. Cell-state transitions and collective cell movement generate an endoderm-like region in gastruloids. *Elife*, 11:e59371, 2022.

39. Harold M McNamara, Sabrina C Solley, Britt Adamson, Michelle M Chan, and Jared E Toettcher. Recording morphogen signals reveals origins of gastruloid symmetry breaking. *bioRxiv*, 2023.

40. Nicolaas Godfried Van Kampen. *Stochastic processes in physics and chemistry*, volume 1. Elsevier, 1992.

41. Patrick S Stumpf, Rosanna CG Smith, Michael Lenz, Andreas Schuppert, Franz-Josef Müller, Ann Babtie, Thalia E Chan, Michael PH Stumpf, Colin P Please, Sam D Howison, et al. Stem cell differentiation as a non-markov stochastic process. *Cell Systems*, 5(3):268–282, 2017.

42. Arthur D Lander, Kimberly K Gokoffski, Frederic Y M Wan, Qing Nie, and Anne L Calof. Cell lineages and the logic of proliferative control. *PLoS biology*, 7(1):e1000015, 2009.

43. Jonathan W Armond, Krishanu Saha, Anas A Rana, Chris J Oates, Rudolf Jaenisch, Mario Nicodemi, and Sach Mukherjee. A stochastic model dissects cell states in biological transition processes. *Scientific reports*, 4(1):3692, 2014.

44. Sameeran Kunche, Huaming Yan, Anne L Calof, John S Lowengrub, and Arthur D Lander. Feedback, lineages and self-organizing morphogenesis. *PLoS computational biology*, 12(3):e1004814, 2016.

45. David A Turner, Penelope C Hayward, Peter Baillie-Johnson, Pau Rué, Rebecca Broome, Fernando Faunes, and Alfonso Martinez Arias. Wnt/β-catenin and fgf signalling direct

the specification and maintenance of a neuromesodermal axial progenitor in ensembles of mouse embryonic stem cells. *Development*, 141(22):4243–4253, 2014.

46. Melody Merle, Leah Friedman, Corinne Chureau, Armin Shoushtarizadeh, and Thomas Gregor. Precise and scalable self-organization in mammalian pseudo-embryos. *Nature Structural & Molecular Biology*, pages 1–7, 2024.

47. Philip L Townes and Johannes Holtfreter. Directed movements and selective adhesion of embryonic amphibian cells. *Journal of experimental zoology*, 128(1):53–120, 1955.

48. Malcolm S Steinberg and Masatoshi Takeichi. Experimental specification of cell sorting, tissue spreading, and specific spatial patterning by quantitative differences in cadherin expression. *Proceedings of the National Academy of Sciences*, 91(1):206–209, 1994.

49. Ramsey A Foty, Cathie M Pfleger, Gabor Forgacs, and Malcolm S Steinberg. Surface tensions of embryonic tissues predict their mutual envelopment behavior. *Development*, 122(5):1611–1620, 1996.

50. Robert David, Olivia Luu, Erich W Damm, Jason WH Wen, Martina Nagel, and Rudolf Winklbauer. Tissue cohesion and the mechanics of cell rearrangement. *Development*, 141(19):3672–3682, 2014.

51. Tony Y-C Tsai, Mateusz Sikora, Peng Xia, Tugba Colak-Champollion, Holger Knaut, Carl-Philipp Heisenberg, and Sean G Megason. An adhesion code ensures robust pattern formation during tissue morphogenesis. *Science*, 370(6512):113–116, 2020.

52. Hans-Jörg Fehling, Georges Lacaud, Atsushi Kubo, Marion Kennedy, Scott Robertson, Gordon Keller, and Valerie Kouskoff. Tracking mesoderm induction and its specification to the hemangioblast during embryonic stem cell differentiation. 2003.

53. Nicola Gritti, Jia Le Lim, Kerim Anlaş, Mallica Pandya, Germaine Aalderink, Guillermo Martínez-Ara, and Vikas Trivedi. MOrgAna: accessible quantitative analysis of organoids with machine learning. *Development*, 148(18), 09 2021. dev199611.

54. Sébastien Le Digabel. Algorithm 909: Nomad: Nonlinear optimization with the mads algorithm. *ACM Transactions on Mathematical Software (TOMS)*, 37(4):1–15, 2011.

55. Samuel L Wolock, Romain Lopez, and Allon M Klein. Scrublet: computational identification of cell doublets in single-cell transcriptomic data. *Cell systems*, 8(4):281–291, 2019.

56. F Alexander Wolf, Philipp Angerer, and Fabian J Theis. Scanpy: large-scale single-cell gene expression data analysis. *Genome biology*, 19:1–5, 2018.

Cell fate modelling

Here we use a heuristic approach considering cells transition between different states (*41–44*). We will simplify the branched lineage process obtained using single-cell RNA sequencing analysis in Fig. 2 by combining states 2 and 3 into a single state (B) and states 4, 5 and 6 into a single state (C). Therefore, we will assume unbranched unidirectional transitions between states A (state 1), B and C. Next, we describe the different models discussed in the main text.

First-order kinetics

The simplest possible model is to assume each cell evolves through those states with rates that are unaffected by the presence of other cells. Such a model reads:

$$\dot{\phi}_A = -p\phi_A \tag{S1}$$

$$\dot{\phi}_B = p\phi_A - q\phi_B \tag{S2}$$

$$\dot{\phi}_C = q\phi_B \tag{S3}$$

where ϕ_i is the fraction of cells in state i and $\phi_A + \phi_B + \phi_C = 1$. For the case $p \neq q$, the solution to this linear model reads:

$$\phi_A(t) = \phi_A^0 e^{-pt} \tag{S4}$$

$$\phi_B(t) = (1-\phi_A^0)e^{-qt} + \frac{\phi_A^0 p}{q-p}\left(e^{-pt} - e^{-qt}\right) \tag{S5}$$

where $\phi_A^0 \equiv \phi_A(0)$ and $\phi_C(t) = 1 - \phi_B(t) - \phi_A(t)$. For the particular case $p = q$, the solution takes the form:

$$\phi_A(t) = \phi_A^0 e^{-pt} \tag{S6}$$

$$\phi_B(t) = e^{-pt}\left[1 + \phi_A^0(pt-1)\right] \tag{S7}$$

This extremely simple model can successfully reproduce a maximum in the T+ population over time; however, due to its linear nature, it cannot reproduce the nonlinear dependence on ϕ

observed experimentally in Fig. 1D.

Cell-cell signalling

Next we consider the case of cell-cell signalling in the cellular aggregate. Let us define the transition rates $\Gamma_{AB}(\phi_i;\mu)$, $\Gamma_{BC}(\phi_i;\mu)$, where μ indicates the type of feedback that applies to the transition ($\mu = +1$, positive; $\mu = 0$, no feedback; $\mu = -1$, negative) and i is the cell population that drives the feedback. For simplicity, we will exclude the models where two different cell populations feedback to the same transition (e.g. state A and B, driving a postive feedback on transition AB). A given model is defined by the type of feedback for transitions AB and BC (μ and ν, respectively) and the cell population that controls such feedbacks (i and j, respectively):

$$\dot{\phi}_A = -\Gamma_{AB}(\phi_i;\mu)\phi_A \tag{S8}$$

$$\dot{\phi}_B = \Gamma_{AB}(\phi_i;\mu)\phi_A - \Gamma_{BC}(\phi_j;\nu)\phi_B \tag{S9}$$

$$\dot{\phi}_C = \Gamma_{BC}(\phi_j;\nu)\phi_B \tag{S10}$$

where $\Gamma_{AB}(\phi_i;\mu) = p\Gamma(\phi_i;\mu)$, $\Gamma_{BC}(\phi_j;\nu) = q\Gamma(\phi_j;\nu)$ and Γ is a modulation of the transition rate according to the feedback taking the form:

$$\Gamma(\phi_i;\mu) = \delta_{\mu,0} + \left(\frac{\phi_i\delta_{\mu,1}/K + \delta_{\mu,-1}}{1+\phi_i/K}\right) \tag{S11}$$

where δ_{ij} corresponds to a Kronecker delta. We can rewrite the equations in a dimensionless form by rescaling time by one of the transition rates (e.g. p) such that we obtain:

$$\dot{\phi}_A = -\Gamma(\phi_i;\mu)\phi_A \tag{S12}$$

$$\dot{\phi}_B = \Gamma(\phi_i;\mu)\phi_A - \alpha\Gamma(\phi_j;\nu)\phi_B \tag{S13}$$

$$\dot{\phi}_C = \alpha\Gamma(\phi_j;\nu)\phi_B \tag{S14}$$

where $\alpha = q/p$ and we have the constraint $\phi_C(t) = 1 - \phi_A(t) + \phi_B(t)$.

Solution for the case $\mu = -1$, $\nu = -1$.

In this case it is possible to solve the dynamics analytically given that the dynamics of A is uncoupled from the dynamics of B and C. The set of equations in this case reads:

$$\begin{aligned} \dot{\phi}_A &= -\frac{\phi_A}{1+\phi_A/K} \\ \dot{\phi}_B &= \frac{\phi_A - \alpha\phi_B}{1+\phi_A/K} \end{aligned} \tag{S15}$$

and the solution reads:

$$\begin{aligned} \phi_A(t) &= KW\left(\frac{\phi_0}{K}e^{-t+\phi_0/K}\right) \\ \phi_B(t) &= \frac{1}{\alpha-1}\left[\phi_A(t) + (-1+\alpha-\alpha\phi_0)\left(\frac{\phi_A(t)}{\phi_0}\right)^{\alpha}\right], \quad \alpha \neq 1 \\ \phi_B(t) &= \frac{\phi_A(t)}{\phi_0}\left[1-\phi_0+\phi_0\log\left(\frac{\phi_0}{K}\right) - \phi_0\log\left(\frac{\phi_A(t)}{K}\right)\right], \quad \alpha = 1 \end{aligned} \tag{S16}$$

where $\phi_0 \equiv \phi_A(0) = 1 - \phi_B(0)$ and W is the Lambert W function.

Supplementary Figures

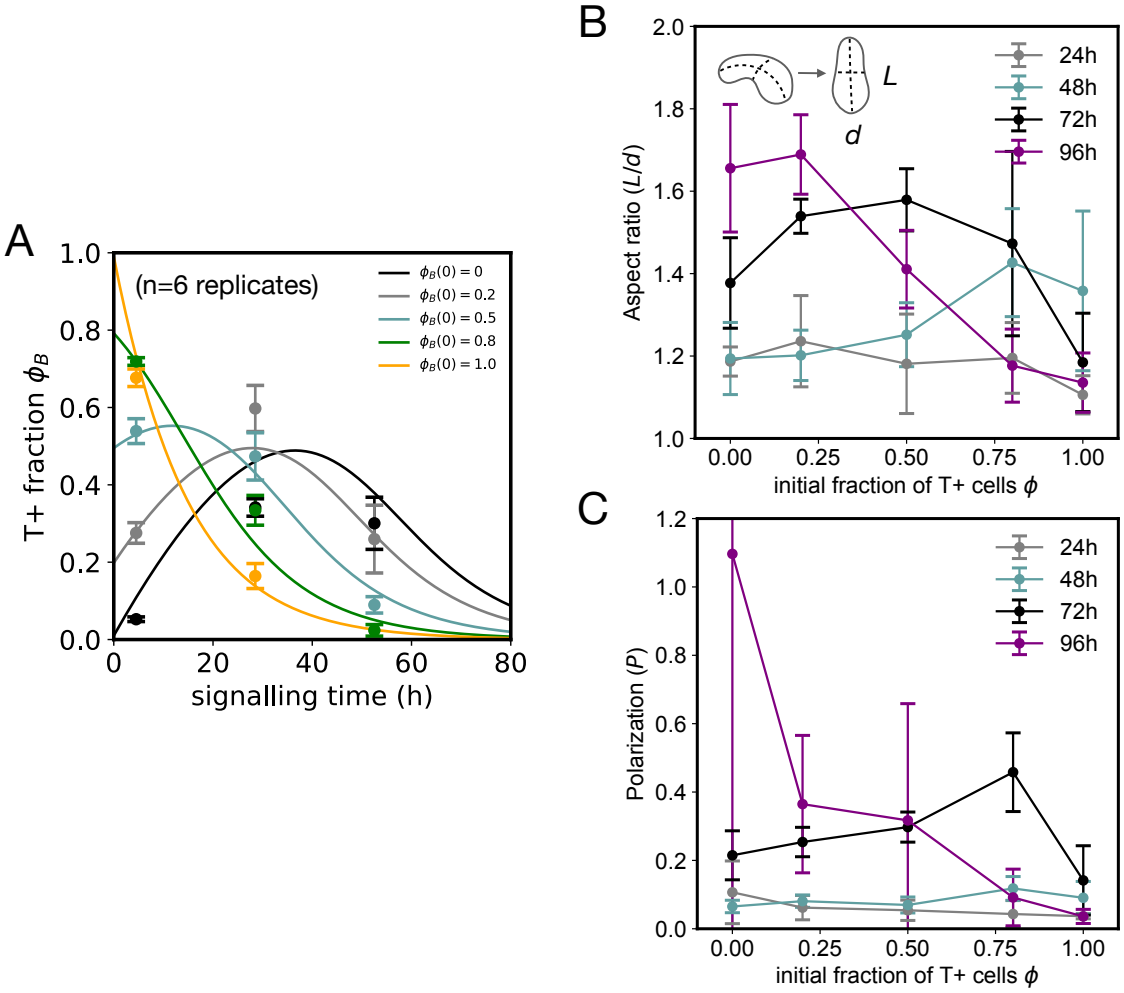

Figure S1: **Initial T+ fraction ϕ_B controls the timing of gastruloid polarisation and elongation**. A) Time evolution of the T+ fraction for different initial conditions. The data is the same as in Fig. 1B,C with the solid lines indicating the corresponding fits to the model. Mean $\pm$ 2 $\times$ SEM. $n = 6$ replicates. B,C) Polarisation and elongation of gastruloids for different initial T+ fractions ϕ. The polarisation P was calculated as the first dipolar moment (see Methods). Mean $\pm$ SD, $n = 5$ replicates.

Annotation	Genes
Epiblast/Pluripotency	Nanog+, Sox2+
Posterior Epiblast	Nanog+, T+
Posterior Primitive Streak	Nanog-, T+
Anterior Mesoderm	Eomes+, Gata6+, Mesp1+
Posterior Mesoderm	Aldh1a2+, Tbx6+
Endoderm	Eomes+, Gata6+, Sox17+

Table S1: **Annotation markers**.

Antibody	Company	Catalogue number	Dilution
anti-E-Cadherin	Cell Signaling	3195	1:2000
anti-N-cadherin	Abcam	ab18203	1:2000
anti-α-catenin	Merck (Sigma)	T6199	1:1000

Table S2: **Primary antibodies used for the Western Blots**.

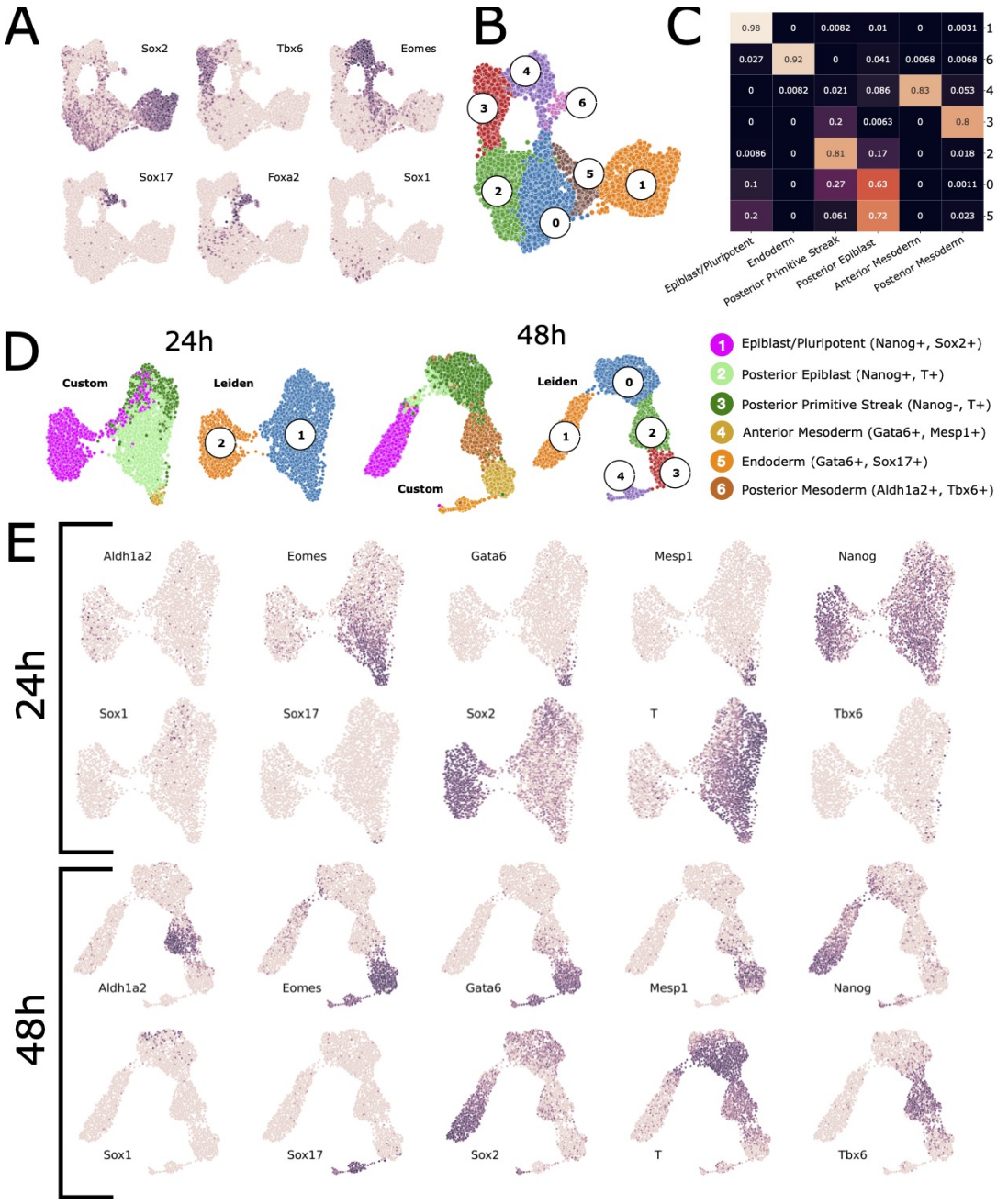

Figure S2: **Additional information of the scRNA-seq dataset presented in the main text**. A) UMAPs of integrated analysis (24 hpa and 48 hpa) colored by marker genes used for the annotation of the clusters, in addition to the markers shown in Fig. 2. B) UMAP of the integrated analysis (24 hpa and 48 hpa) with the identified leiden clusters. C) Confusion matrix normalised by columns showing the consistency of annotation between the annotated clusters in the independent analysis and the integrated analysis cluster annotations. D) UMAPs of the independent analysis at 24 hpa and 48 hpa of the dataset, with the obtained clusters annotated. E) Marker genes expressed over the UMAPs of the time-independent analyses.

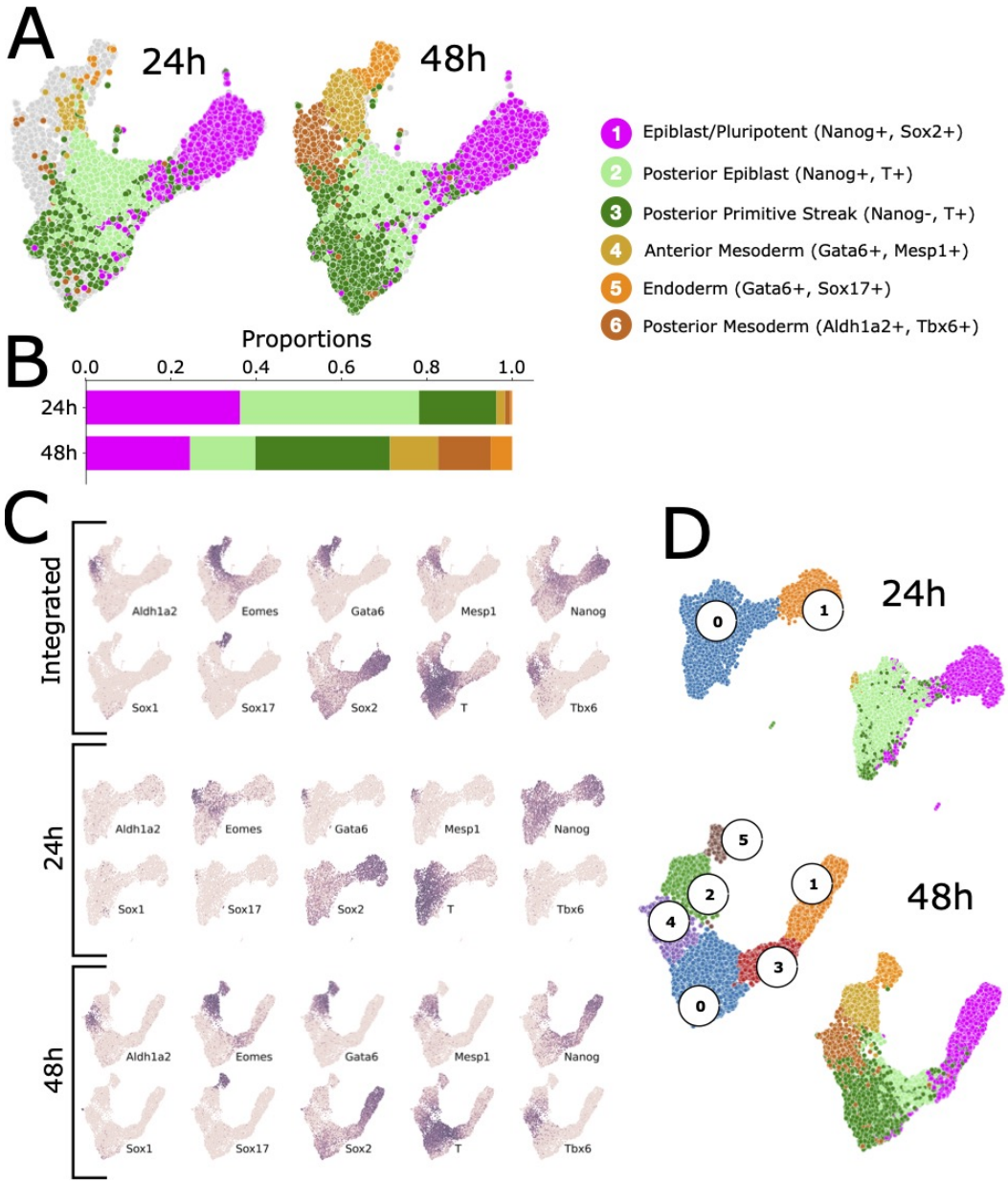

Figure S3: **scRNA-seq analysis of independent gastruloid replicas at 24 hpa and 48 hpa**. A) UMAPs of the integrated analysis of the 24 hpa and 48 hpa datasets with the annotated clusters. B) Proportion of cells per annotation and time point. C) UMAPs of the integrated and independent analysis at 24 hpa and 48 hpa of the dataset, with the marker genes expression color-coded. D) UMAPs of the independent analysis per time-point, showing the leiden clustering and the automatic annotation method.

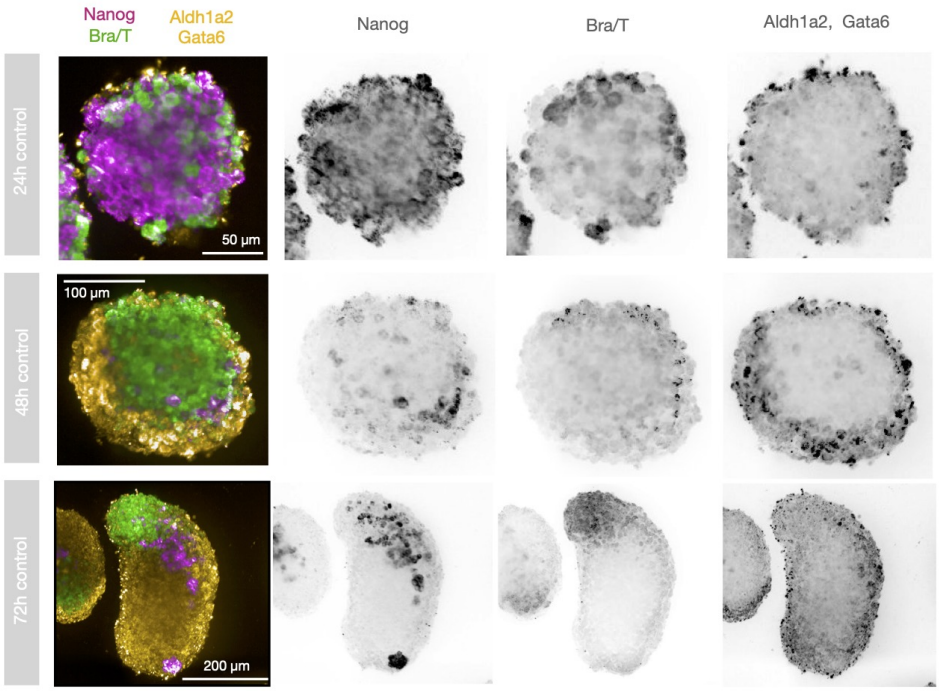

Figure S4: **HCR stainings of gastruloids**. Second replicate as a control. The dynamic range is the same in all images. The images correspond to a maximum intensity projection. T: 488 nm, Nanog: 647 nm, Aldh1a2, Gata6: 546 nm.

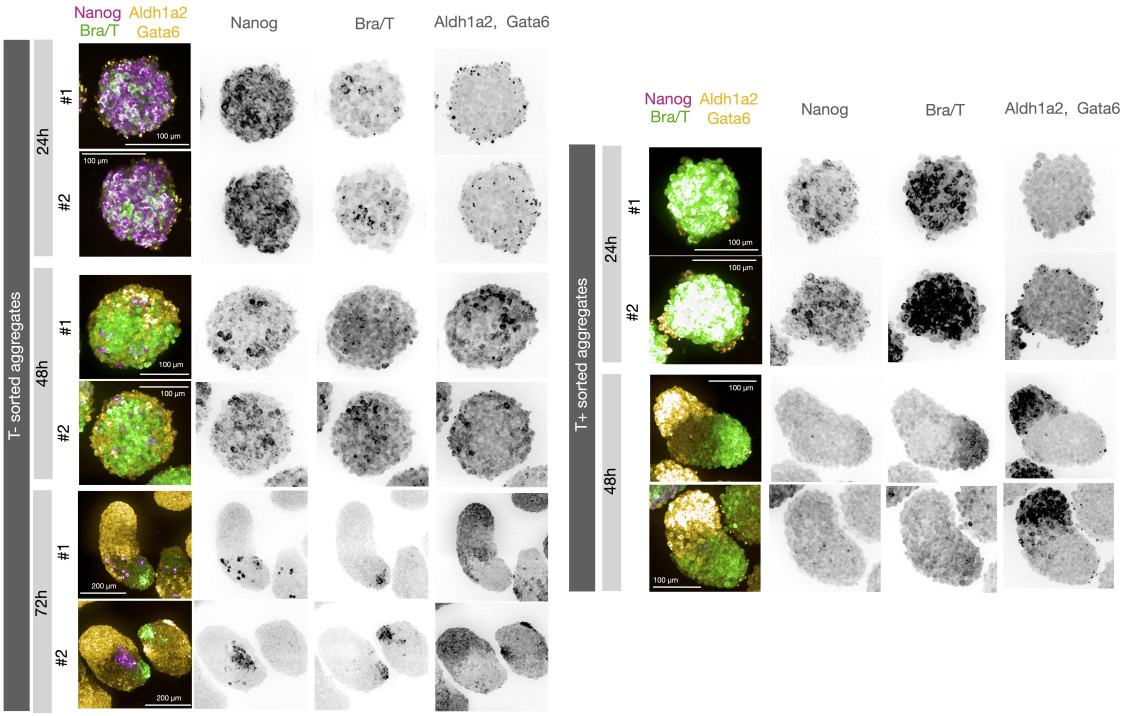

Figure S5: **HCR stainings of T- and T+ sorted aggregates**. The dynamic range is the same in all images and the staining protocol was applied in parallel to the T+ and T- aggregates. The images correspond to a maximum intensity projection. T: 488 nm, Nanog: 647 nm, Aldh1a2, Gata6: 546 nm. No clear signal of the markers could be observed for 72 hpa T+ aggregates.

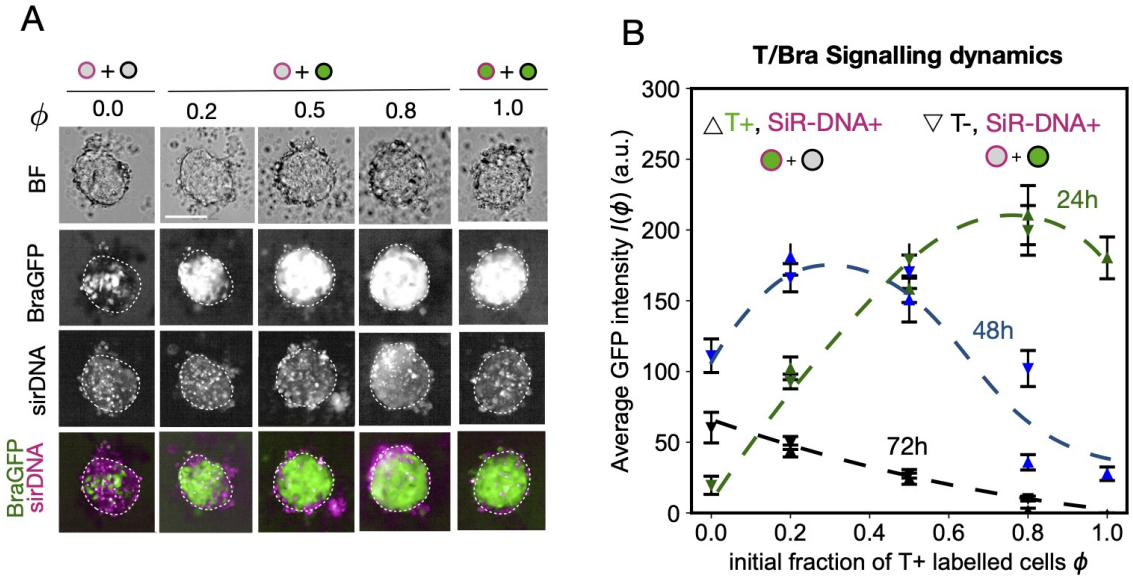

Figure S6: **3D mES cell aggregates at 24 hpa for different initial fractions** ϕ. A) Confocal imaging of 3D mES cell aggregates. The panel shows brightfield (BF), T (GFP) and SiR-DNA signals. The images correspond to maximum intensity projections. Scale bar: 100 μm. B) Average GFP intensity $I(\phi)$ versus the initial fraction of T+ labelled cells ϕ adding SiR-DNA to the T+ (upper triangles) or the T- (lower triangles) populations. T dynamics in the aggregates remained unaffected upon the addition of SiR-DNA. Dashed lines are only a guide to the eye. Error bars correspond to SEM.

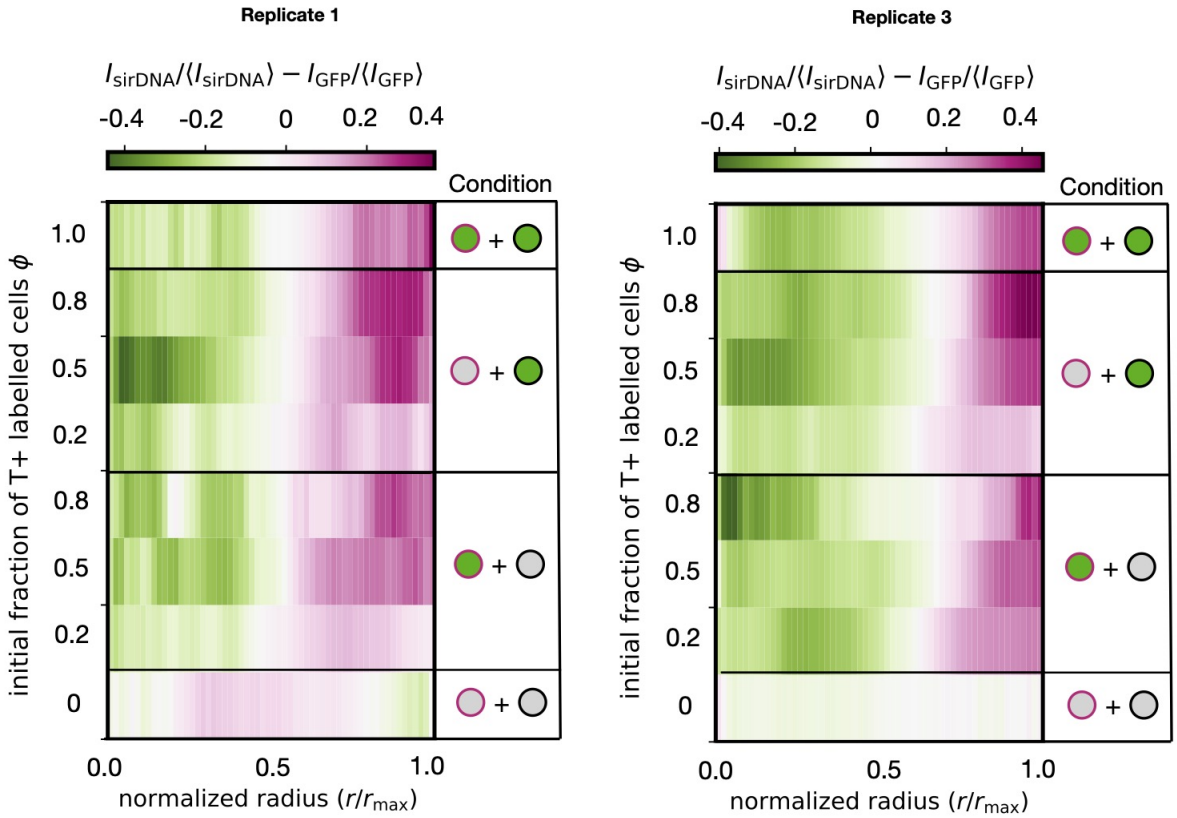

Figure S7: **Radial profiles mESC aggregates**. Colormaps of the radial profile for different starting fractions of T+ (ϕ) and different conditions. Replicates 1 and 3 are shown, while Replicate 2 is shown in Fig. 3D. The replicates were done on different days using different batches of cells.

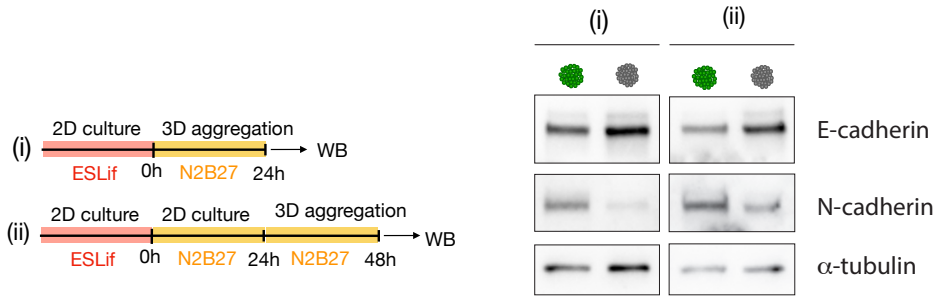

Figure S8: **Cadherin protein levels in T+ and T- aggregates**. FACS sorted T+ and T- aggregates (600 cells) were cultured for 24 hpa (i) or 48 hpa (ii) in N2B27 prior to the lysate. Western blots showed differential protein levels of E and N-cadherin. N-and E-cadherin levels were higher in T+ and T- aggregates, respectively.

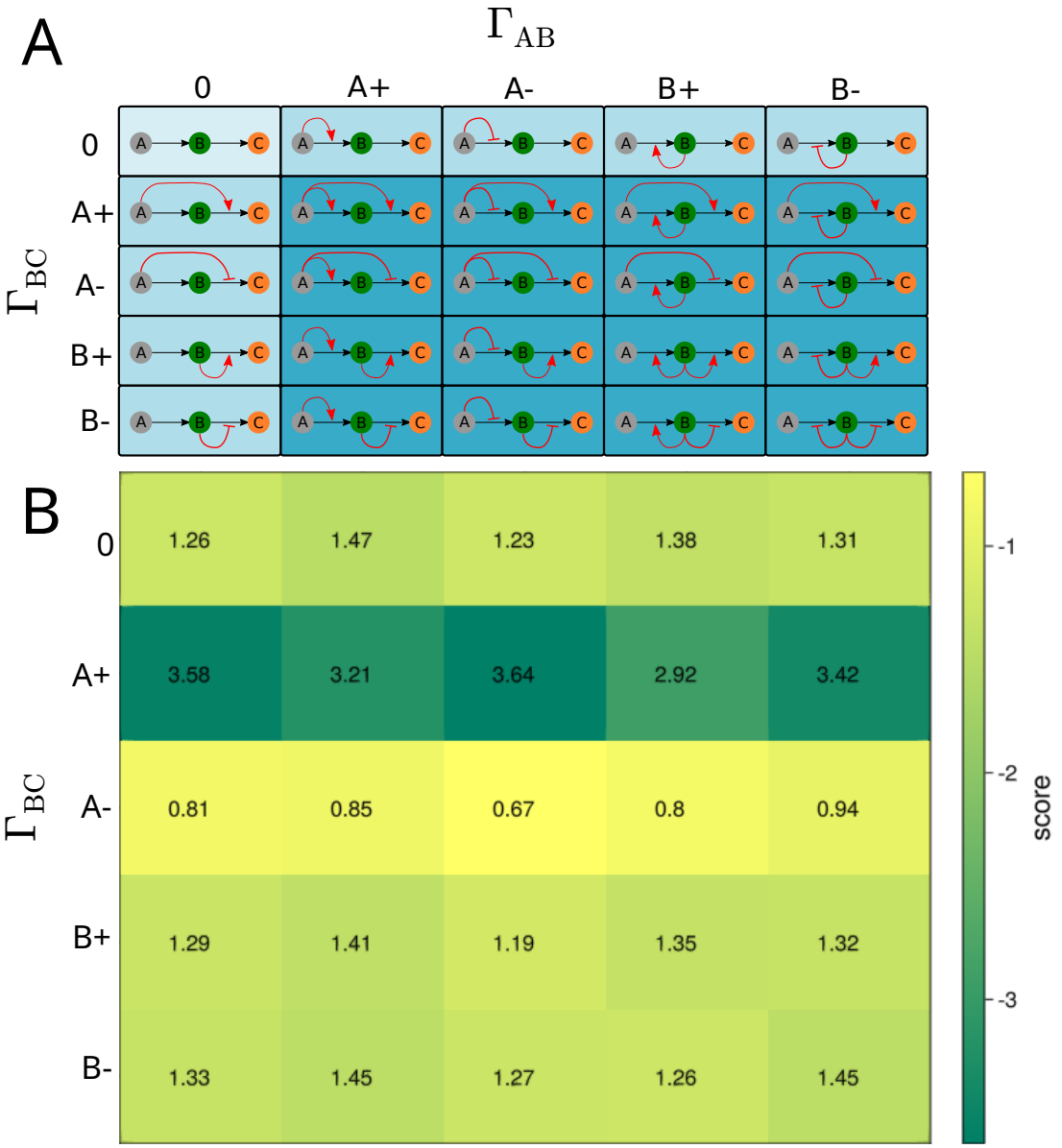

Figure S9: **Cell-cell signalling models**. A) Possible cell-cell signalling models of up to two distinct regulation arrows, on the transition ratios between cell states for the three-state model. B) Loss score of the fit to the data for each of the models described in panel (A). The lower the score, the better the fit to the model. "A+/A-" or "B+/-" indicates that states A or B up-regulate/down-regulate a certain cell fate transition. "0" indicates that a certain cellular state is not regulating a cell fate transition.

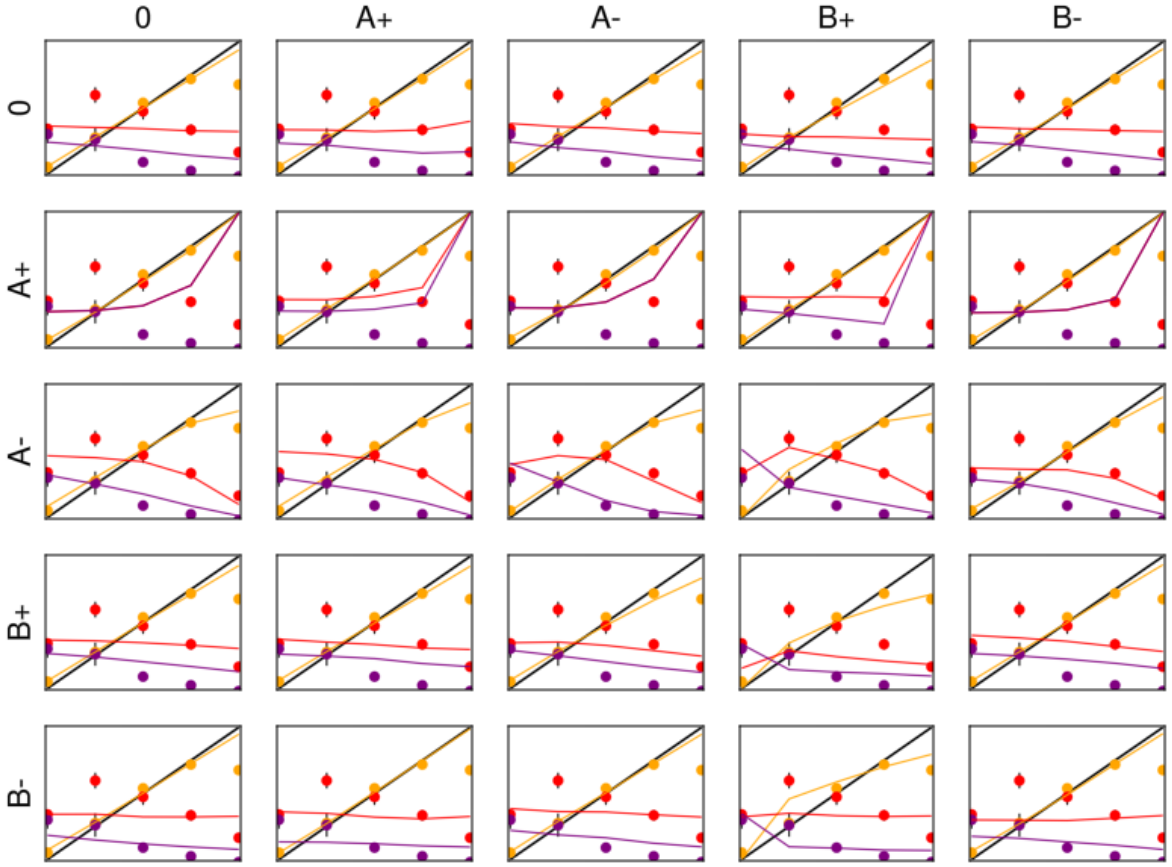

Figure S10: **Best fitting over possible cell-cell communication models**. Solid lines displaying the trends of the best parameter fitting for each model, described in Supplementary Figure S9. Filled circles correspond to the experimental data in Fig. 1D (Yellow: 24 hpa, Red: 48 hpa and Purple: 72 hpa).

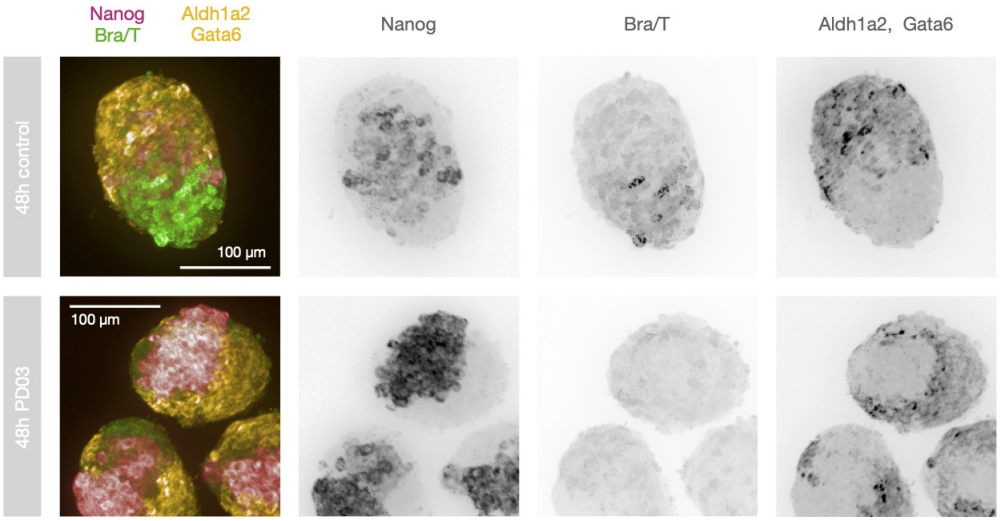

Figure S11: **HCR stainings of 48 hpa cell aggregates for the case $\phi_B(0) = 0.5$ and 1μM PDO3 inhibition from 24 hpa to 48 hpa**. We observe the lack of Bra/T signal in the inhibited aggregates, showing that the A to B transition is halted upon PDO3 treatment. T: 488 nm, Nanog: 647 nm, Aldh1a2, Gata6: 546 nm.

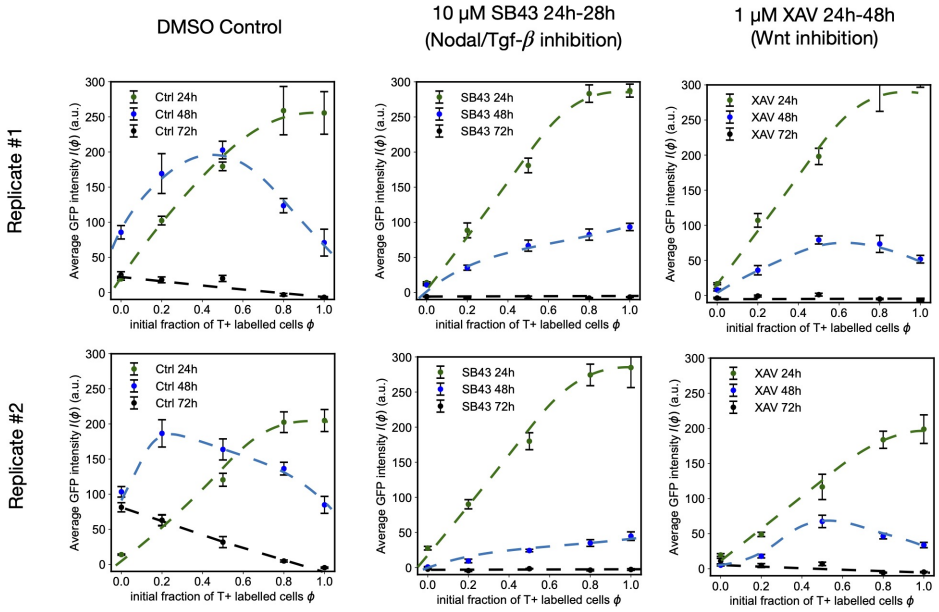

Figure S12: **Effect upon the inhibition of Wnt and Nodal/Tgf-β pathways on the evolution of the fraction of cells expressing T at 24, 48 and 72 hpa**. The Nodal/Tgf-β pathway was inhibited using 10 μM SB43 and the Wnt pathway was inhibited by using 1 μM XAV. Both inhibitors where incubated from 24 to 48 hpa. Mean $\pm$ SEM. Dashed lines are only a guide to the eye.